THESIS FOR THE DEGREE OF LICENTIATE OF ENGINEERING

Degenerate and nondegenerate Josephson parametric oscillators for quantum information applications

ANDREAS BENGTSSON

Department of Microtechnology and Nanoscience (MC2)
CHALMERS UNIVERSITY OF TECHNOLOGY
Göteborg, Sweden 2017

Degenerate and nondegenerate Josephson parametric oscillators for quantum information applications
ANDREAS BENGTSSON

Technical Report MC2-377
ISSN 1652-0769

Quantum Device Physics Laboratory
Department of Microtechnology and Nanoscience (MC2)
Chalmers University of Technology
SE-412 96 Göteborg
Sweden
Telephone: +46 (0)31-772 1000

Cover:
Quadrature histograms of nondegenerate parametric oscillations.

Chalmers Reproservice
Göteborg, Sweden 2017

Degenerate and nondegenerate Josephson parametric oscillators for quantum information applications
Thesis for the degree of Licentiate of Engineering
ANDREAS BENGTSSON
Department of Microtechnology and Nanoscience (MC2)
Chalmers University of Technology

Abstract

Parametric oscillations are well studied phenomena, with applications in amplification, quantum optics, and quantum information processing. They can occur as a parameter of a system, such as the resonant frequency, is being modulated or "pumped" by an external field. A nonlinearity of the system can then transfer power from the pumping frequency to two frequencies called signal and idler. When the signal falls within a resonance, and when the pump amplitude exceeds an instability threshold, parametric oscillations occur. When signal and idler fall within the same resonance, the pumping is called degenerate.

Due to somewhat different implementations, in combination with rich nonlinear physics, the details of the parametric oscillations can differ in different systems. In this work, we expand on the research done on parametric oscillations using a superconducting microwave resonator with a tunable boundary condition. Previously, a degenerate Josephson parametric oscillator (JPO) has been demonstrated by modulation of this boundary condition at twice the resonator's resonant frequency. We further use the JPO to implement a novel read-out method for a superconducting qubit. Moreover, we demonstrate a different, nondegenerate regime of the JPO, which we denote the NJPO, by modulating the frequency at the sum of two resonant frequencies of a multimode resonator.

Both the JPO qubit read-out and the NJPO have applications within quantum information processing. The perhaps most promising platform for quantum information processing is represented by the circuit-QED architecture with superconducting resonators and artificial atoms, where the two lowest atomic levels represent the qubit. We make these circuits using lithographic techniques, and control and measure them at low temperature using microwaves. The qubit's state is fragile and difficult to read out with high fidelity. To this end, we have developed a method based on the JPO, in which the qubit state is mapped onto a zero-amplitude or a large-amplitude state of the JPO. We achieved a large contrast (185 ± 15 photons), therefore eliminating the need for a following quantum-limited parametric amplifier. Our readout fidelity was 81.5 %, and by carefully modeling we can distinguish fidelity loss from the qubit and the readout, respectively. This analysis displays an actual readout fidelity of 98.7 %.

An alternative model for quantum computing is based on continuous variables, and uses harmonic oscillators instead of qubits. Entangled states, which can be used as quantum resources, can then be created, for example, by two-mode squeezing of the oscillator ground state. The state of the NJPO produces correlated oscillations in its two modes, which might be useful for continuous-variable quantum computing. In this work we fully characterize the classical properties of the NJPO, and show good quantitative agreement with a theoretical model.

Keywords: Parametric oscillations, multimode, superconducting circuits, SQUID, quantum information, circuit quantum electrodynamics

Acknowledgements

First of all, a big thank you to my supervisor Jonas Bylander for your great support and leadership. This thesis and our results wouldn't exist without your guidance, attention to details, and knowledge. Secondly, I wish to express me gratitude to Philip Krantz and Michaël Simoen for helping me so much in the beginning. Two people that contributed a lot to this work is Per Delsing and Vitaly Shumeiko, thank you for all your support with both experiments and theory, without you the results wouldn't have been nearly as good and well presented. Also, thank you to Jonathan Burnett for proof reading and all the work we have done together for the past year. Hopefully, some great results are soon to come!

None of the devices in this thesis would exist without the excellent support of the staff at the Nanofabrication Laboratory. My gratitude to Niclas Lindvall, Henrik Fredriksen, Mats Hagberg, and Johan Andersson for all the help.

It doesn't help to have great devices unless you have some way to mount them in your dilution refrigerator. Lars Jönsson helped us machine all the parts for the sample boxes, mounting plates, coils, *etc.* Sorry for all the urgent jobs with late notice! Your work is very much appreciated.

The administrative support from Susannah Carlsson is invaluable! Thank you for all the help to make sure that being a PhD student at QDP is as easy as possible. You really allow us to focus on the research, knowing that the rest is taken care of.

To my family and friends, thank you for all the support! Finally, a big thank you to all current and former employees at QDP for making it a great place to work in.

Andreas Bengtsson, Falkenberg, Christmas Day 2017

Symbols & Abbreviations

Abbreviations

SQUID	Superconducting quantum interference device
cQED	Circuit quantum electrodynamics
CPW	Coplanar waveguide
JPO	Josephson parametric oscillator
NJPO	Nondegenerate Josephson parametric oscillator
JPA	Josephson parametric amplifier
HEMT	High-electron-mobility transistor
SNTJ	Shot-noise tunnel junction
AWG	Arbitrary waveform generator
LO	Local oscillator
IF	Intermediate frequency
SNR	Signal-to-noise ration

Constants

e	Electron charge
$\hbar$	Reduced Planck constant
k_B	Boltzmann constant
c	Speed of light

Superconductivity

φ	Phase difference across Josephson junction
I_c	Critical current of a Josephson junction
L_J	Josephson junction inductance
L_sq	Josephson inductance of the SQUID
C_sq	SQUID capacitance
Φ	Magnetic flux
Φ_0	Magnetic flux quantum
Φ_DC	DC magnetic flux

Resonator parameters

S_{11}	Reflection coefficient
Z_{in}	Impedance of a piece of transmission line
Z_{r}	Impedance of the resonator including the coupling capacitance
C_{c}	Coupling capacitance
Z_C	Impedance of the coupling capacitor
C_0	Capacitance per unit length
L_0	Inductance per unit length
α	Real part of the wave propagation constant
β	Imaginary part of the wave propagation constant
Z_0	Characteristic impedance of the transmission line
v_{ph}	Phase velocity
d	Resonator CPW length
γ_{l}	SQUID inductance participation ratio
γ_{c}	SQUID capacitance participation ratio
k_n	Wave number of mode n
ω_n	Resonant frequency of mode n
$\omega_{\lambda/4}$	Bare resonant frequency (without SQUID)
Q_{c}	Coupling quality factor
Q_{i}	Internal quality factor
Q	Total quality factor
λ	Wavelength

Parametric oscillations

α_n	Duffing parameter of mode n
α_{g}	Geometric mean of the mode nonlinearities
ϵ	Effective pump strength
δ	Pump detuning
δ_n	Detection detuning
ζ_n	Effective pump detuning
Δ_0	Oscillation frequency detuning
A_n	Intramode field
B_n	Incoming field
C_n	Outgoing field
Γ_{n0}	Coupling rate of mode n
Γ_n	Total damping rate of mode n
Γ	Geometric mean of the mode dampings
G	Gain
BW	Bandwidth

Qubit parameters

ω_r	Resonator frequency
ω_a	Qubit frequency
Δ	Qubit-resonator detuning
g	Qubit-resonator coupling
H	Hamiltonian
$\hat{a}$	Harmonic oscillator annihilation operator
$\sigma_{\pm}$	Raising and lowering operators for the qubit
$\|n\rangle$	n^{th} qubit level
χ	Dispersive shift
T_1	Qubit relaxation time
F	Readout fidelity

Other

T	Temperature
ω	Angular frequency
V	Voltage
I	Current

List of publications

This thesis is based on the work contained in the following papers:

Paper A A. Bengtsson, P. Krantz, M. Simoen, I. M. Svensson, B. H. Schneider, V. Shumeiko, P. Delsing, and J. Bylander. Nondegenerate parametric oscillations in a tunable superconducting resonator. *To be submitted to Physical Review B*

Paper B P. Krantz, A. Bengtsson, M. Simoen, S. Gustavsson, V. Shumeiko, W. Oliver, C. Wilson, P. Delsing, and J. Bylander. Single-shot read-out of a superconducting qubit using a Josephson parametric oscillator. *Nature Communications* **7**, 2016

Other papers that are outside the scope of this thesis:

Paper I S. R. Sathyamoorthy, A. Bengtsson, S. Bens, M. Simoen, P. Delsing, and G. Johansson. Simple, robust, and on-demand generation of single and correlated photons. *Physical Review A* **93**: 063823, 2016

Paper II I. M. Svensson, M. Pierre, W. Wustmann, P. Krantz, A. Bengtsson, G. Johansson, J. Bylander, V. Shumeiko, and P. Delsing. Microwave photon generation in a doubly tunable superconducting resonator. *To be published in Journal of Physics: Conference Series*

Paper III I.-M. Svensson, A. Bengtsson, P. Krantz, J. Bylander, V. Shumeiko, and P. Delsing. Period-tripling subharmonic oscillations in a driven superconducting resonator. *Physical Review B* **96**: 174503, 2017

Paper IV J. Burnett, A. Bengtsson, D. Niepce, and J. Bylander. Noise and loss of superconducting aluminium resonators at single photon energies. *To be published in Journal of Physics: Conference Series*

Contents

Thesis

1

Introduction

Superconducting circuits and devices [7, 8] are today found in a variety of systems, such as MRI and MEG machines at hospitals, particle accelerators, power grids, and many more. There are three main features that make superconducting circuits so versatile and useful. Firstly, the absence of electrical resistance allows for very low loss electrical circuits, as well as the generation of high magnetic fields. Secondly, tunable nonlinear elements can be implemented, and used, for example, as amplifiers, mixers, and detectors. Finally, superconducting circuits are very sensitive to their environment, enabling a large range of different detectors for telescopes, small magnetic fields, *etc.*

Here, we use superconducting circuits for quantum information processing, which will be discussed later. During the last two decades, superconducting circuits have played a large role in the development of what is now the circuit quantum electrodynamics (cQED) architecture [9, 10]. In other words, the study of light-matter interactions at the level of quanta of energy using circuits. In cQED there are three main building blocks. The first is the resonator. A typical example of a resonator is the LC circuit. A resonator can be seen as a storage for energy, and is characterized by its resonant frequency and by its quality factor, which quantifies for how long energy can be stored. In cQED, the resonator is implemented using superconductors to achieve high quality factors.

The second block is the superconducting quantum interference device (SQUID) [11]. The SQUID, consisting of two superconducting Josephson tunnel junctions connected in parallel, forming a loop that threads a magnetic flux, is essentially a tunable nonlinear inductance. The tunability allows for precise and rapid modulation of different circuit parameters, such as resonant frequencies [12] and couplings [13]. The nonlinearity of the Josephson junctions, and the fact that it can be made strong, is what allows for the generation of nonclassical states to study quantum phenomena.

The third and final block is the quantum bit (qubit). A qubit is a two-level system, analog to a bit in a classical computer. However, the qubit can be in a coherent superposition of its two levels, and entangled with other qubits. Moreover, a qubit can be used as an artificial atom. The artificial atom can be used to study how light and atoms interact. The benefits of using circuits and not real atoms are that it is easier to isolate and manipulate a circuit, and that is easier to engineer its properties.

1.1 Parametric and nonlinear effects

Parametric pumping refers to the pumping (modulation) of one of the parameters of a system. In the case of a resonator there are two possibilities, either to modulate the damping or the resonant frequency. When placing a SQUID at the current antinode of the resonator, its resonant frequency will depend on the magnetic flux through the SQUID. By modulating the magnetic field with a sinusoidal signal, and therefore the resonant frequency, different parametric effects such as amplification [14] and frequency conversion [15] can be realized.

The SQUID also introduces a nonlinearity in the resonator. Nonlinear dynamical systems are popular in textbooks, where effects such as harmonic generation, bifurcation, and chaos are studied [16, 17].

In this work, a phenomenon called parametric oscillation is studied and utilized. By frequency modulating a resonator at twice its resonant frequency, and with a large amplitude, the ground state of the resonator becomes unstable, and therefore the resonator starts to oscillate at its resonant frequency. These oscillations are said to be self-sustained, since there is no external drive of the system at the resonant frequency. Parametric oscillations have been observed in variety of systems, such as optical and microwave cavities [18, 19]. We demonstrate a different regime by using a multimode resonator and a frequency modulation at the sum of two resonant frequencies. This regime is referred to as nondegenerate parametric oscillations.

1.2 Quantum computation

Quantum bits are the fundamental building blocks for quantum computers, and superconducting qubits are one of the most promising architectures for building such a system [20, 21]. A quantum computer is envisioned to be able to solve problems that are today intractable on classical computers, such as prime factorization and quantum simulation of molecules. For each specific problem, a quantum algorithm needs to be found that not only utilize the quantum properties of the qubits, but also yields the correct result when measuring the qubits' states. [22]. To build a successful quantum computer, several criteria need to be fulfilled [23], which are related to, among other things, coherence, control, and readout.

In this work, we study a method for reading out the state of a superconducting qubit using a parametric oscillator. There are two important criteria for the readout, it should be quantum nondemolition (QND) and single shot. QND refers to that after the measurement, the qubit should be in the eigenstate corresponding to the measured eigenvalue [24]. A single shot measurement yields the correct state every time, and can be quantified with a fidelity, *i.e.* the probability of yielding the correct state.

Another architecture for quantum computing is based on continuous variables (CV) where harmonic oscillators (resonators) replace the qubits [25]. Harmonic oscillators have an infinite parameter space, in contrast to qubits which have two energy levels. However, a harmonic oscillator is usually thought of as a classical system. So to do quantum information processing, nonclassical states of the harmonic oscillator are created, such

as superpositions of Fock states [26], entangled two-mode squeezed states [27–29], and multi-photon cat states [30]. In the creation of these states, parametric phenomena play a large role.

Nondegenerate parametric oscillations have shown both two- and three-mode entanglement in the optical regime. The microwave nondegenerate parametric oscillations demonstrated here have an important qualitative similarity to the optical ones, namely a continuous degeneracy of the oscillator state. This degeneracy should lead to large fluctuations under the effect of vacuum noise, and as a result of this, the state might be non-Gaussian [31]. A non-Gaussian state is necessary for universal quantum computing with continuous variables [32].

1.3 Thesis outline

This thesis introduces and summarizes the work of two papers. Chapter 2 introduces some of the necessary theory for understanding the superconducting devices used. Brief descriptions of how the devices are fabricated and measured are provided.

Chapter 3 treats the self-sustained parametric oscillations. The theoretical framework used is briefly outlined for both degenerate and nondegenerate parametric oscillations. It also summarizes the main experimental results regarding the demonstration of nondegenerate parametric oscillations in Paper A.

Chapter 4 covers the basics of superconducting qubits and how they are controlled and read out using the dispersive coupling regime. Then, the method of reading out a qubit's state using a parametric oscillator with high fidelity is demonstrated, which is the results from Paper B. An important part of that paper was to understand the origin of the fidelity loss, which was done using a Monte-Carlo simulation.

Chapter 5 summarizes the main findings of this work and gives some outlook on future work.

2

Superconducting microwave resonators

Microwave resonators are fundamental parts of many electrical circuits. Such a resonator can be used to store electromagnetic energy in the microwave regime, to filter noisy signals, to stabilize oscillators, and to achieve high electric fields [33]. Superconductors are often used in applications requiring very low losses (high quality factors), such as in particle accelerators [34], radiation detectors [35], and quantum devices [21]. In quantum physics, the electromagnetic field inside a resonator can be quantized and instead described using particles knows as photons [36]. The quantization of the electromagnetic field leads for example to the presence of vacuum fluctuations, which means that even in its ground state, the resonator is still oscillating.

This work is to a great extent dependent on tunable microwave resonators to achieve parametric oscillations. Moreover, the circuit needs to have low loss, and the resonant frequencies needs to be modulated fast. To achieve all this, all circuit elements are fabricated out of superconductors on the same chip using standard micro- and nano-fabrication techniques. This chapter introduces the basics concepts of superconductivity, transmission lines, and resonators. Then, it is described how tunable and multimode resonators can be implemented. At the end, fabrication and measurements of such devices are described.

2.1 Superconducting circuit elements

As the name suggests, superconductivity is a phenomenon where the conductivity is very large. In fact, it is infinite for direct currents. However, there is a critical current I_c which is the maximum current a superconductor can sustain. The microscopics behind superconductivity is modeled as an effective attractive interaction between the electrons in the material. Two electrons pair up due to this interaction and creates a so-called Cooper pair. Cooper pairs, in contrast to electrons, are bosons, meaning that below the critical temperature T_c they condense into a single ground state. Due to the binding

between two electrons in a Cooper pair, a gap in the density of states is opened where electrons cannot exist. Thus, the Cooper pairs can move without scattering inside the superconductor, yielding zero resistivity. More information about the microscopic theory and superconductivity in general can be found in Ref. [7].

By separating two superconductors via an insulator, a tunneling barrier is created where a Cooper pair can tunnel through without dissipating energy. Therefore, it is possible to draw a current through the barrier without applying any voltage across it. Mathematically, the effect is described by the two Josephson relations

$$I = I_c \sin\varphi, \tag{2.1}$$

$$V = \frac{\hbar}{2e}\frac{\mathrm{d}\varphi}{\mathrm{d}t}, \tag{2.2}$$

where I is the current through the junction, I_c is the critical current, V is the voltage across, φ is the phase difference between the two superconductors, $\hbar$ is the reduced Planck constant, and e is the electron charge. The two equations can be combined by differentiating Eq. (2.1) and inserting it in Eq. (2.2)

$$V = \frac{\hbar}{2e}\frac{1}{I_c\cos\varphi}\frac{\mathrm{d}I}{\mathrm{d}t}. \tag{2.3}$$

Recalling the voltage-current relation for an inductance, $V = L\,\mathrm{d}I/\,\mathrm{d}t$, the Josephson inductance is defined as

$$L_\mathrm{J} = \frac{\hbar}{2e}\frac{1}{I_c\cos\varphi}. \tag{2.4}$$

Two Josephson junctions in a loop, as illustrated in Fig. 2.1 (a), creates a direct current superconducting quantum interference device (DC-SQUID). Any magnetic field through this loop will introduce a circulating current, effectively decreasing the critical current of the SQUID. Assuming identical junctions, *i.e.* the same critical current, Eq. (2.1) modifies to

$$I = 2I_c\cos\left(\pi\frac{\Phi}{\Phi_0}\right)\sin\varphi, \tag{2.5}$$

where Φ is the magnetic flux through the SQUID loop and $\Phi_0 = h/(2e)$ is the magnetic flux quantum. Similarly to the single Josephson junction, a SQUID inductance is defined as

$$L_\mathrm{sq} = \frac{\hbar}{2e}\frac{1}{2I_c|\cos(\pi\Phi/\Phi_0)|\cos\varphi}. \tag{2.6}$$

For a comprehensive review of SQUIDs, see Ref. [11].

Due to the geometry of the Josephson junctions in the SQUID, there is a stray capacitance C_sq in parallel with the SQUID inductance L_sq, which forms an LC resonator. In practice, the resonant frequency of the SQUID is typically 40 GHz. Above this frequency the SQUID behaves more as a capacitance than an inductance; thus any device utilizing the Josephson inductance needs to operate below the this frequency.

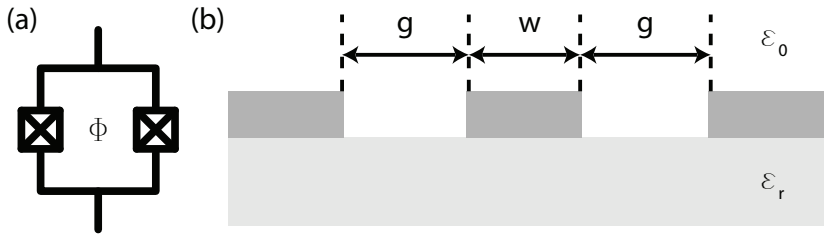

Figure 2.1: *Illustration of some of the components used. (a) SQUID. It consists of two Josephson junctions (represented as squares with crosses) in parallel, forming a loop. Φ denotes the magnetic flux through the loop. (b) A cross section of a co-planar waveguide with a center conductor of width w and gap to ground planes of width g. The conductor and ground planes are located on a substrate with a relative dielectric constant ϵ_r. Above the CPW there is vacuum, with the relative dielectric constant 1.*

2.2 Transmission lines

Transmission lines are used to guide electromagnetic waves from one point to another. There are many different types of transmission lines. For microwaves, the most common ones include coaxial cables, microstrips, and co-planar waveguides. A transmission line can be described mathematically by the telegraph equations [33], where the transmission line is modeled as a chain of discrete components. The input parameters to the telegraph equations are the series inductance per unit length L_0, shunt capacitance per unit length C_0, series resistance per unit length R_0, and shunt conductance per unit length G_0. The complex propagation constant γ for a wave with travelling with the angular frequency ω in the transmission line is $\gamma = \sqrt{(R_0 + j\omega L_0)(G + j\omega C_0)}$. For low loss and high frequency ($R_0 \ll \omega L_0$ and $G_0 \ll \omega C_0$) the propagation constant simplifies to

$$\gamma \approx \frac{1}{2}\left(R\sqrt{\frac{C_0}{L_0}} + G\sqrt{\frac{L_0}{C_0}}\right) + j\omega\sqrt{L_0 C_0} = \alpha + j\beta, \tag{2.7}$$

where α and β are the real and imaginary parts of the propagation constant. In this approximation, the impedance seen by an incoming wave is $Z_0 \approx \sqrt{L_0/C_0}$. The phase velocity of the travelling wave is $v_{\mathrm{ph}} = 1/\sqrt{L_0 C_0} = c/\sqrt{\epsilon_{\mathrm{eff}}}$, where ϵ_{eff} is the effective dielectric constant of the media where the wave travels, implying that $\beta = \omega/v_{\mathrm{ph}}$ and

$$L_0 C_0 = \epsilon_{\mathrm{eff}}/c^2. \tag{2.8}$$

The transmission line used in this work is a co-planar waveguide (CPW) [37], which is used routinely in both normal and superconducting circuits. A CPW consists of a center conductor and two ground planes on a dielectric substrate. The center conductor has a width w, and a gap distance g to the surrounding ground planes, see Fig. 2.1 (b). The two widths w and g, together with the relative dielectric constant ϵ_{r}, determine the inductance and capacitance per unit length.

As discussed above, a transmission line has a characteristic impedance Z_0. The most common characteristic impedance for microwave equipment is $50\,\Omega$, thus the CPW needs

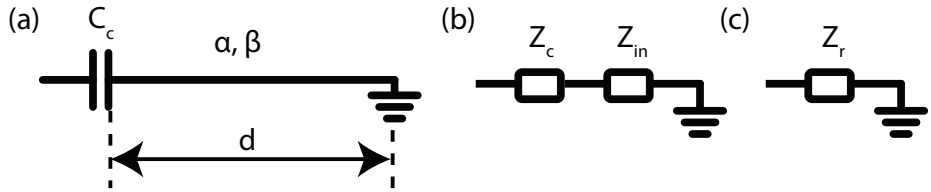

Figure 2.2: *(a) Capacitively coupled quarter wavelength resonator. A piece of transmission line with the complex wave propagation constant $\alpha + j\beta$, is shorted to ground in one end, and capacitively coupled to another transmission line at the other end. The distance d sets the fundamental resonant frequency $\omega_{\lambda/4} = \pi v_{\mathrm{ph}}/2d$. C_c is the coupling capacitance. (b-c) Equivalent impedances models.*

to be designed with the same impedance to avoid reflections at the interfaces. Typically, the effective dielectric constant of a CPW on a substrate with a dielectric constant ϵ_r is $\epsilon_{\mathrm{eff}} \approx (1 + \epsilon_r)/2$. This gives the product L_0C_0 via Eq. (2.8). To get the ratio of L_0 and C_0 one can use either finite-element electromagnetic simulations via commercially available software, or the mathematical tool of conformal mapping to transform the CPW into a geometry where the analytical expression for the capacitance is known [37].

2.3 The quarter wavelength resonator

To realize a microwave resonator, a piece of transmission line can be used. By fixing the length of the transmission line piece, and the two boundary conditions (usually open or grounded), see Fig. 2.2 (a), one can calculate the resulting resonant frequencies. Normally, one of resonator's ends are used to couple the resonator to another transmission line which is used to drive and measure the resonator. Refs. [38–40] cover the derivation of a capacitively coupled transmission line resonator's frequency response. First, the impedance of just the piece of transmission line which constitutes the resonator needs to be found, and re-expressed in terms of quality factors instead of circuit parameters such as inductance, capacitance, and resistance. Since the transmission lines used here are superconductive, a low-loss approximation can be done. Then, the impedance due to the coupling between the resonator and transmission line is introduced, see Fig. 2.2 (b). This slightly modifies the resonant frequency, so the new resonant frequency needs to be found together with the external coupling quality factor. When the full system impedance is determined, Fig. 2.2 (c), the reflection coefficient of that impedance is easily calculated.

The input impedance Z_{in} of a transmission line at a distance d from a load impedance Z_{L} is [33]

$$Z_{\mathrm{in}} = Z_0 \frac{Z_{\mathrm{L}} + Z_0 \tanh\left[(\alpha + j\beta)d\right]}{Z_0 + Z_{\mathrm{L}} \tanh\left[(\alpha + j\beta)d\right]}. \tag{2.9}$$

For a short circuit, $Z_{\mathrm{L}} = 0$, Eq. (2.9) becomes

$$Z_{\mathrm{in}} = Z_0 \tanh\left[(\alpha + j\beta)d\right] = Z_0 \frac{\tanh \alpha d + j \tan \beta d}{1 + j \tan \beta d \tanh \alpha d} = Z_0 \frac{1 - j \tanh \alpha d \cot \beta d}{1 + j \tanh \alpha d - j \cot \beta d}, \tag{2.10}$$

Assuming a resonant frequency $\omega_{\lambda/4}$ for a quarter wavelength $d = \lambda/4$ gives

$$\beta d = \frac{\omega d}{v_{\mathrm{ph}}} = \frac{\omega_{\lambda/4} d}{v_{\mathrm{ph}}} + \frac{\Delta d}{v_{\mathrm{ph}}} = \frac{\pi}{2} + \frac{\pi}{2}\frac{\Delta}{\omega_{\lambda/4}}, \tag{2.11}$$

where $\Delta = \omega - \omega_{\lambda/4}$ is the detuning from the resonant frequency. To get rid of the different trigonometric and hyperbolic terms in Eq. (2.10), Eq. (2.11) is used together with the assumption that $\Delta/\omega_{\lambda/4} \ll 1$, which yields

$$\cot \beta d = \cot\left(\frac{\pi}{2} + \frac{\pi}{2}\frac{\Delta}{\omega_{\lambda/4}}\right) = -\tan\frac{\pi}{2}\frac{\Delta}{\omega_{\lambda/4}} \approx -\frac{\pi}{2}\frac{\Delta}{\omega_{\lambda/4}}. \tag{2.12}$$

The internal Q-factor of the transmission line is defined as $Q_{\mathrm{i}} = \beta/2\alpha$. For low loss transmission lines, which is the case for superconducting co-planar waveguides, $\tanh \alpha d = \tanh \beta d/2Q_{\mathrm{i}} \approx \beta d/2Q_{\mathrm{i}}$. In combination with Eq. (2.10) and Eq. (2.12), this gives an approximate input impedance without trigonometric and hyperbolic terms

$$Z_{\mathrm{in}} \approx Z_0 \frac{1 + j\frac{\beta d}{2Q_{\mathrm{i}}}\frac{\pi}{2}\frac{\Delta}{\omega_{\lambda/4}}}{\frac{\beta d}{2Q_{\mathrm{i}}} + j\frac{\pi}{2}\frac{\Delta}{\omega_{\lambda/4}}} \approx \frac{Z_0}{\frac{\pi}{4Q_{\mathrm{i}}}\left(1 + \frac{\Delta}{\omega}\right) + j\frac{\pi}{2}\frac{\Delta}{\omega_{\lambda/4}}} \approx \frac{4Z_0Q_{\mathrm{i}}/\pi}{1 + j2Q_{\mathrm{i}}\frac{\Delta}{\omega_{\lambda/4}}}. \tag{2.13}$$

The only circuit parameter remaining is the characteristic impedance Z_0, the rest have been absorbed in $\omega_{\lambda/4}$ and Q_{i}.

To interact with the resonator, a coupling between the resonator and a second transmission line is needed. In this work, a capacitive coupling to a transmission line with the characteristic impedance Z_0 is used. The series impedance of the resonator and the coupling is

$$Z_{\mathrm{r}} = Z_{\mathrm{in}} - \frac{j}{\omega C_c} = \frac{4Z_0Q_{\mathrm{i}}/\pi}{1 + j2Q_{\mathrm{i}}\frac{\Delta}{\omega_{\lambda/4}}} - \frac{j}{\omega C_c}, \tag{2.14}$$

where C_c is the coupling capacitance. To translate C_c into a coupling quality factor Q_c, one can use the definition of the quality factor $Q_c = E\omega_{\lambda/4}/P$, where E is the total energy stored in the resonator, and P is the power lost through the capacitor. On resonance, half of the energy in the resonator is stored in the electric field. Therefore, integration of the voltage along the resonator can be used in the formula for the electric energy stored in a capacitor $CV^2/2$ to find the total energy in the resonator

$$E = 2\int_0^d \frac{1}{2}C_0\left[V_{\mathrm{rms}}\sin\left(\frac{2\pi}{4d}x\right)\right]^2 \mathrm{d}x = \frac{1}{2}C_0V_{\mathrm{rms}}^2 d = \frac{\pi V_{\mathrm{rms}}^2}{4\omega_{\lambda/4}Z_0}, \tag{2.15}$$

where V_{rms} is the voltage at the coupling capacitor, and I_{rms} is the current through the capacitor. The same current will flow in the transmission line, implying that the power lost through the capacitor into the transmission line is $P = I_{\mathrm{rms}}^2 Z_0 = Z_0 V_{\mathrm{rms}}^2 \omega_{\lambda/4}^2 C_c^2$. Therefore, the coupling quality factor is

$$Q_{\mathrm{c}} = \frac{E}{P/\omega_{\lambda/4}} = \frac{\pi}{4Z_0^2\omega_{\lambda/4}^2 C_c^2} \implies \omega_{\lambda/4}C_c = \sqrt{\frac{\pi}{4Z_0^2 Q_{\mathrm{c}}}}. \tag{2.16}$$

The impedance of the resonator and the coupling, Eq. (2.14), can be rewritten in terms of Q_c using Eq. (2.16) in the following way

$$Z_{\mathrm{r}} = \frac{4Z_0 Q_{\mathrm{i}}/\pi}{1 + j2Q_{\mathrm{i}}\frac{\Delta}{\omega_{\lambda/4}}} - j2Z_0\sqrt{\frac{Q_{\mathrm{c}}}{\pi}}. \tag{2.17}$$

Due to the loading of the resonator via the capacitive coupling, the resonant frequency is changed. The resonance condition is given by $\mathrm{Im}(Z_{\mathrm{r}}) = 0$, evaluating to

$$\frac{\Delta}{\omega_{\lambda/4}} = -\frac{1}{\sqrt{\pi Q_{\mathrm{c}}}}. \tag{2.18}$$

Therefore, the loaded resonant frequency has to be redefined accordingly, giving the final resonator impedance close to the resonant frequency

$$Z_{\mathrm{r}} \approx 2Z_0\sqrt{\frac{Q_{\mathrm{c}}}{\pi}}\frac{2Q_{\mathrm{i}}\frac{\Delta}{\omega_{\lambda/4}} - j}{1 + j2Q_{\mathrm{i}}\left(\frac{\Delta}{\omega_{\lambda/4}} - 1/\sqrt{\pi Q_{\mathrm{c}}}\right)}. \tag{2.19}$$

In this work, the measured quantity is the reflection coefficient of the resonator, which evaluates to [33]

$$S_{11} = \frac{Z_{\mathrm{r}} - Z_0}{Z_{\mathrm{r}} + Z_0} \approx \frac{\Delta - j\left(\frac{\omega_{\lambda/4}}{2Q_{\mathrm{i}}} - \frac{\omega_{\lambda/4}}{2Q_{\mathrm{c}}}\right)}{\Delta - j\left(\frac{\omega_{\lambda/4}}{2Q_{\mathrm{i}}} + \frac{\omega_{\lambda/4}}{2Q_{\mathrm{c}}}\right)} = \frac{\Delta - i(\Gamma_i - \Gamma_0)}{\Delta - i(\Gamma_i + \Gamma_0)}, \tag{2.20}$$

where the internal (external) loss rates are defined as $\Gamma_i = \omega_{\lambda/4}/2Q_i$ ($\Gamma_0 = \omega_{\lambda/4}/2Q_c$). Finally, the total loss rate is $\Gamma = \Gamma_i + \Gamma_0$, equivalent to $1/Q = 1/Q_{\mathrm{i}} + 1/Q_{\mathrm{c}}$, where Q is the total quality factor.

2.4 Frequency-tunable resonators

The resonators described so far are fixed in frequency, which in some applications is sufficient. However, in this work, resonators with a tunable resonant frequency are needed. Not only do they need to be tunable, but for parametric pumping the resonant frequency needs to be modulated faster than the resonant frequency itself. To achieve fast frequency tunability, a DC-SQUID is placed at the grounding point of the resonator where the current is maximum [12], as shown in Fig. 2.3 (a). The inductance of the SQUID, L_{sq}, gives an additional phase shift, which is equivalent to an increase in the resonator's electrical length. The fundamental resonant frequency ω_1 of the SQUID-terminated resonator can be approximated by [41]

$$\omega_1(F) \approx \frac{\omega_{\lambda/4}}{1 + \gamma_{\mathrm{l}}/|\cos(\pi\Phi/\Phi_0)|}, \tag{2.21}$$

where $\omega_{\lambda/4}$ is the resonant frequency without the SQUID, and γ_{l} is the inductive participation ratio defined as $\gamma_{\mathrm{l}} = L_{\mathrm{sq}}/L_0 d$.

Incorporation of a SQUID into the resonator does not only enable frequency modulation, it also adds a nonlinearity to the system due to the cosine dependence between current through and phase across the junction. By Taylor expanding Eq. (2.5) to third order, the relation becomes

$$I = 2I_c \cos\left(\pi \frac{\Phi}{\Phi_0}\right) \sin(\varphi) \approx 2I_c \cos\left(\pi \frac{\Phi}{\Phi_0}\right) (\varphi - \varphi^3/6). \tag{2.22}$$

The cubic term is known as the Duffing term, or Kerr term in optics. The presence of a cubic term leads to nonlinear effects, for example a lower effective critical current for higher currents. This causes a power dependent frequency shift of the resonator, which can be quantified by α_n, the amount of negative frequency shift per photon in the resonator [42].

2.5 Multimode resonators

So far, only the fundamental mode of the quarter wavelength resonator has been examined. However, as the co-planar waveguide resonator is of the distributed type, higher harmonics also exist. As long as the voltage profile fulfills the given boundary condition, the voltage can have arbitrary number of nodes inside the piece of transmission line. For the tunable resonator described above, the modes exist at $\omega_n \approx (2n-1)\omega_1$, where $n = 1, 2, 3, ...$ is the mode number. This relation is only approximate since the phase drop across the SQUID modifies the mode frequencies differently for each mode, creating an anharmonic spectrum. The spectrum of the tunable multimode resonator can be found be solving the dispersion equation [43, 44]

$$k_n d \tan k_n d = \frac{|\cos(\pi\Phi/\Phi_0)|}{\gamma_1} - k_n d\gamma_c, \tag{2.23}$$

where $k_n d = \pi\omega_n/2\omega_{\lambda/4}$ and $\gamma_c = C_{sq}/C_0 d$ is the capacitive participation ratio. In Fig. 2.3 (b), the six lowest modes calculated using Eq. (2.23), together with experimental data for three of the modes, are seen as a function of magnetic flux through the SQUID loop. Each mode of the resonator is characterized by its resonant frequency ω_n, external loss rate Γ_{n0}, total loss rate Γ_n, and Duffing nonlinearity α_n.

2.6 Fabrication

To realize the circuits just described, modern micro- and nano-fabrication techniques are used. The resonator and the transmission lines consist of co-planar waveguide with gaps between the center conductor and the ground planes on the order of micrometers. To create tunable resonators, SQUIDs and on-chip flux lines are needed. A typical device is depicted in Fig. 2.4. The Josephson junctions of the SQUIDs have features down to 100 nm.

For the dielectric substrate, two materials are used. Either (0001) sapphire or intrinsic high-resistivity (100) silicon. These materials are chosen due to their low dielectric

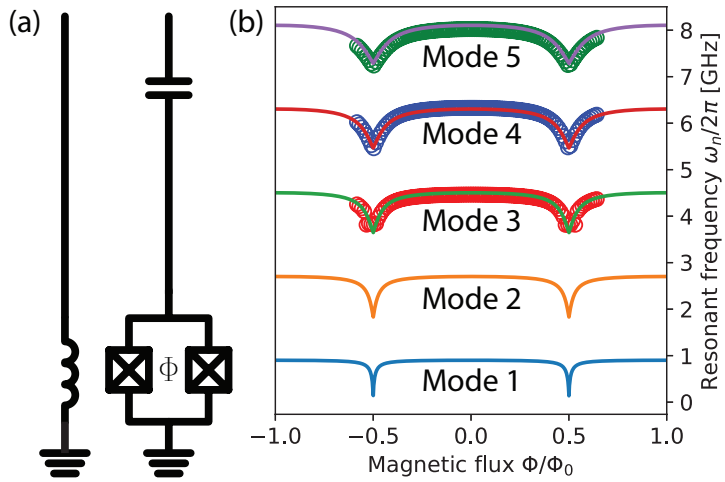

Figure 2.3: *Overview of a tunable multimode resonator. (a) The SQUID terminated resonator, with an inductively coupled microwave line that can be used to change the magnetic flux* Φ *through the SQUID loop. (b) Resonant frequencies of the six lowest modes, as a function of magnetic flux through the SQUID loop. These frequencies are calculated for a resonator with* $\omega_{\lambda/4}/2\pi = 919\,\mathrm{MHz}$, $\gamma_\mathrm{l} = 0.02$, *and* $\gamma_\mathrm{c} = 0.009$. *Open circles are experimental data, showing good agreement with the theoretically calculated frequencies.*

losses, yielding high internal quality factors of the resonators [45]. Even though sapphire has lower losses than silicon in the bulk, the dominating surface losses brings them to comparable levels [46]. Moreover, from a fabrication point of view, both substrates have their advantages and disadvantages. For example, sapphire is insulating which makes it charge up during electron-beam lithography (EBL) and scanning-electron microscopy (SEM), on the other hand it is difficult to etch niobium selectively to silicon.

An overview of the fabrication processes is presented below. For more detailed information about the fabrication on the devices used in this work, see Appendix A and Ref. [47].

First, the substrate wafer is cleaned thoroughly in solvents to remove organic residues on the surface. In the case of silicon, a hydroflouric acid (HF) dip is performed just prior to loading into the deposition system. The HF removes the native surface oxide known to host a large density of charged two-level fluctuators, which are responsible for a large part of the surface loss [48]. However, the oxide is regrown quickly if the bare silicon is exposed to air [49]. Therefore, it is important to load into the vacuum of the deposition system within minutes of the HF dip.

The superconductor used for the resonators in this work is niobium. A thin film of niobium (80-90 nm) is sputtered onto the substrate using a near UHV, DC magnetron, sputtering system. The deposited niobium covers the entire surface of the wafer. Subsequently, the niobium is patterned using either electron-beam lithography or direct-write laser (DWL) lithography system. The pattern is transferred to the niobium using an inductively-coupled reactive ion plasma of NF_3.

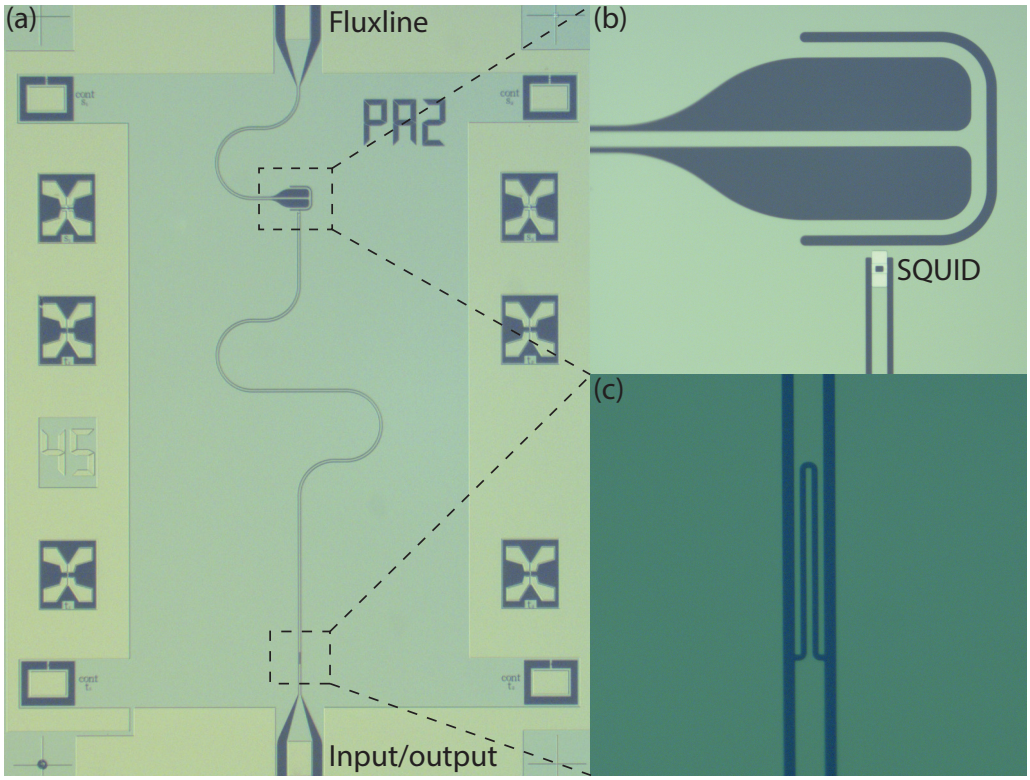

Figure 2.4: *Micrographs of a typical tunable resonator. (a) Full sample with the on-chip fluxline at the top, and the input/output port with the coupling capacitor at the bottom. The resonator is meandered to fit in a smaller chip. This chip is 5x7 mm. (b) SQUID together with the inductive coupling between the fluxline and the SQUID loop. (c) Coupling capacitor.*

The last part of the fabrication is to create the SQUIDs and divide the wafer into individual chips. This is done by first using electron-beam lithography on a bilayer resist system. The pattern is two rectangles, separated by a short distance, creating a free standing bridge. Before development, the wafer is diced into $5\,\mathrm{mm}^2 \times 7\,\mathrm{mm}^2$ chips using a diamond-blade saw. Then, the resists on the chips are developed separately using two different chemicals. This allows for precise control of the undercut size, which is crucial for having a free-standing bridge. One chip at the time is then inserted into a electron-beam evaporator only equipped with aluminum targets, which minimizes the probability of cross contamination. Inside the vacuum chamber there is also an ion gun used to etch the native niobium oxide before evaporation. A sequence of two evaporations with an oxidation step in between, creates the three layers of the Josephson junctions. The first evaporation is done from an angle $-\theta$, forming the first electrode of the Josephson junctions. Then the top part of the electrode is oxidized with a controlled oxygen pressure inside the chamber, thus creating the insulating part. Lastly, a second evaporation is done from an angle θ, overlapping the oxidized aluminum, forming the second electrode. The excess aluminum is finally lifted off.

2.7 Cryogenic measurements

To experimentally find the resonant frequencies and their associated quality factors, a vector network analyzer (VNA) is used to measure the reflection coefficient S_{11} as a function of frequency. By fitting the measured reflection coefficients to Eq. (2.20), the resonant frequency, and internal and external quality factors can be extracted. However, due to the small physical cross sections of the resonators, their resistance per unit length R_0 is large when the niobium is not superconducting and therefore the resonators cannot be measured at room temperature. To achieve the cryogenic temperatures needed, a commercially available dilution refrigerator is used. The chip containing the resonator is wirebonded to a printed circuit board inside a connectorized gold-plated copper box, which is mounted on the mixing chamber of the refrigerator. Cooling to a temperature of 3 K is done using the second stage of a pulse-tube cryocooler [50]. However, close to T_c (9.3 K for niobium) there is still a large population of quasiparticles (unpaired electrons), yielding microwave losses [51]. Therefore, a temperature $T_c/10$ is typically required to avoid this effect.

Moreover, to observe quantum phenomena, the temperature needs to be much lower than the thermal energy corresponding to the frequency of the resonator. For example, $\hbar\omega/k_B \approx 300\,\mathrm{mK}$, where $\omega/2\pi = 6\,\mathrm{GHz}$. Ideally the temperature should then be below 30 mK. This is achieved by the dilution unit in the refrigerator. A phase boundary in a mixture of helium-3 and helium-4 is used to reach temperatures around 10 mK [52], allowing measurements almost unaffected by thermal fluctuations and quasiparticles.

To change the magnetic flux through the SQUIDs, there are two possibilities, an external coil, or an on-chip flux line. The external coil is mounted on the outside of the sample box, ideally providing a uniform magnetic field field across the chip. However, this field cannot be modulated fast. For fast modulation, an on-chip flux line provides magnetic fields locally to the SQUID and can be modulated by a microwave signal.

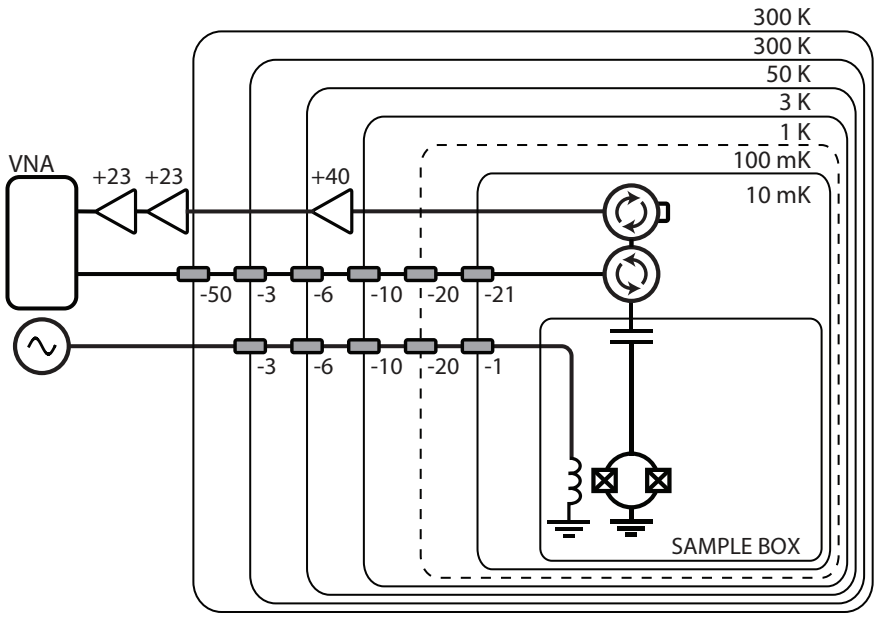

Figure 2.5: *Schematic of a typical cryogenic and microwave setup for measuring tunable superconducting resonators. Each solid box corresponds to a radiation shield at the indicated temperature. The dashed box only shows the temperature of that stage since there is no radiation shield there. The attenuators (grey rectangles) are thermalized at the indicated temperature stages. Two circulators are used to provide isolation between the thermal noise of the amplifier and the resonator.*

The microwave setup can be divided into two parts: inside and outside of the cryostat. An illustration of the setup inside the cryostat is seen in Fig. 2.5. The input signals are attenuated on their way down from room temperature to 10 mK. This serves three purposes: first, it thermally anchors the lines to the different stages of the cryostat. Secondly, it yields the appropriate signal powers at the resonator input. Finally, it also attenuates the thermal noise generated at the different temperature stages inside the cryostat. The attenuation of the input line is 110 dB, whereof 60 dB is inside the cryostat. For the flux line, the attenuation is 40 dB, all inside the cryostat. Additionally, there is extra attenuation in the microwave components such as cables, filters, and circulators, due to their finite insertion loss.

In this work, the resonators used are one port devices. However, for practical reasons, the input and output to the resonator is separated into two lines. To achieve this, a microwave circulator is used. The input line is attenuated as described above, whereas the output line is not attenuated. Moreover, the output path contains amplifiers to bring the power up to measurable levels. The amplification is done in two stages: first, by a high electron mobility transistor, low noise amplifier (LNA), with a noise temperature of 2 K mounted at the 3 K stage of the cryostat. The second stage is outside the cryostat, where two cascaded amplifiers boost the signal even further. If the gain of the LNA is high enough, its noise temperature determines the total system noise. The gain of the LNA used is 40 dB, and the room temperature ones are 23 dB each.

3

Parametric oscillations in tunable microwave resonators

The first observation of self-sustained parametric oscillations was done in a second-order-nonlinear ($\chi^{(2)}$) optical cavity, by pumping the cavity at twice its resonant frequency (degenerate case) [18]. When the pump amplitude exceeded an instability threshold, oscillations were observed at half the pump frequency. Pumping at the sum of two resonant frequencies (nondegenerate case) lead to correlated oscillations in both modes [53]. Entanglement between the two modes was demonstrated [54], and also extended to include the pump mode, yielding a three-mode-entanglement [55].

In the microwave domain, frequency-tunable superconducting resonators based on Josephson junctions are versatile tools. Two parallel Josephson junctions form a superconducting quantum interference device (SQUID), which acts as a magnetic-flux-tunable inductance, therefore enabling frequency modulation via inductively coupled microwaves [12]. When a frequency-tunable resonator is driven parametrically, below the threshold amplitude, it provides amplification at the quantum limit [14, 56, 57] and entangled two-mode squeezed states [27, 29]. Above the threshold amplitude, parametric oscillations occur [19].

For a theoretical analysis of parametric oscillations in a SQUID terminated resonator, a field amplitude formalism was developed in Refs. [42, 44]. There, Langevin equations for the field in the resonator mode, A_n, was derived. The following two sections summarize the key results of that work.

The measurement results at the end of this chapter are solely on nondegenerate parametric oscillations. However, the theory for the degenerate case is relevant for understanding and the single-shot qubit readout chapter. Experimental results for degenerate parametric oscillations is found in Ref. [19].

3.1 Degenerate parametric oscillations

Parametric pumping at twice a resonant frequency is referred to as degenerate pumping. This is effectively three-wave mixing, where the signal and idler are at the same frequency. In a quantum picture, it can be seen as a split of one pump photon with frequency ω_p into two equal signal photons in mode n of frequency $\omega_n = \omega_p/2$, implying that there is always an even number of photons produced at ω_n. When the pump strength overcomes an instability threshold set by the mode loss rate Γ_n, the resonator starts oscillating at ω_n even in absence of an external drive at that frequency.

In Ref. [42], the equation of motion for the intramode amplitude A_n for degenerate parametric pumping in a rotating frame at $\omega_p/2 = \omega_n + \delta$ is derived as

$$i\dot{A}_n + \left(\delta + \alpha_n |A_n|^2\right) A_n + \epsilon A_n^* + i\Gamma_n A_n = \sqrt{2\Gamma_{n0}} B_n, \tag{3.1}$$

where $\delta = \omega_p/2 - \omega_n$ is the pump detuning, ϵ is the parametric pump strength, α_n is the Duffing parameter, B_n is an external drive field, and A_n^* denotes the complex conjugate of A_n. Due to the external coupling with strength Γ_{n0}, the intramode fields couples into the transmission line. Therefore, the outgoing field C_n is related to the incoming and intramode fields as

$$C_n = B_n - j\sqrt{2\Gamma_{n0}} A_n. \tag{3.2}$$

The normalization of the fields is such that $|A_n|^2$ is equivalent to the average number of photons in the n^{th} mode; hence $|B_n|^2$ and $|C_n|^2$ are the in- and outgoing photon rates. The term $\alpha_n |A_n|^2$ is effectively increasing δ, equivalent to a lower resonant frequency. This is the Duffing, or Kerr, effect due to the cubic nonlinearity of the current-phase relation of the SQUID.

In the steady state, $\dot{A}_n = 0$, and for no external drive, $B_n = 0$, Eq. (3.1) has three solutions

I. The trivial solution $A_n = 0$. However, it is only stable for $\epsilon < \Gamma_n$ or $|\delta| > \sqrt{\epsilon^2 - \Gamma_n^2}$.

II. The excited state solution $|A_n|^2 = \left(-\delta + \sqrt{\epsilon^2 - \Gamma_n^2}\right)/\alpha_n$. This solution is stable for $\epsilon \geq \Gamma_n$ and $\delta \leq \sqrt{\epsilon^2 - \Gamma_n^2}$.

III. The third solution has the same amplitude and stability as 2, although, its phase is shifted by π radians.

The regions of stability can be visualized by plotting the excited state amplitudes, see Fig. 3.1 (a). In the absence of nonlinearities, the oscillation amplitude would diverge and increase indefinitely. However, due to the Kerr effect, δ increases as the amplitude $|A_n|$ increases, thus stabilizing the oscillations.

The excited state of the degenerate parametric oscillator has two π shifted solutions, see Fig. 3.1(c). Switching between the two states is possible [58] and has been observed [19]. It has been proposed that one could create a coherent superposition of the two states [59], forming a so called Schrödinger's cat state, which is a resource in quantum information processing [60]. The frequency of the parametric oscillations is always centered around $\omega_p/2$, and the frequency width is given by the switching rate between the states.

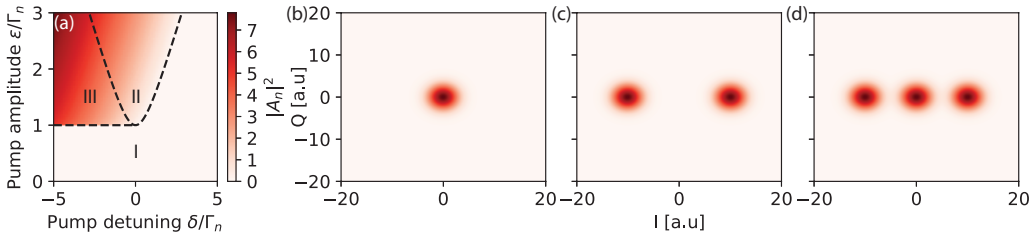

Figure 3.1: *(a) Theoretical steady-state intensities $|A_n|^2$ of a degenerate Josephson parametric oscillator as a function of pump detuning δ and amplitude ϵ. Inside region I, only the ground state is stable (b). In region II, only the excited state is stable (c). Finally, in region III, boths states are stable (d). (b-d) Phase-space distributions for the three different stability regions.*

3.2 Nondegenerate parametric oscillations

Nondegenerate pumping refers to when the pump frequency equals the sum of two resonant frequencies. Then, the signal and idler are separated into two different modes, and the pump frequency is $\omega_p = \omega_n + \omega_m + 2\delta$, where $n \geq 0$ and $m > n$, and δ is the pump detuning. In the quantum picture, the photons are again created in pairs, so that if a photon is detected in mode n, it is certain that there is a photon also in mode m. It is therefore easy to understand that there should be entanglement in such a system.

Similarly to the degenerate case, equation of motions for the intramode fields A_n and A_m can be derived in the corresponding rotating frames $\omega_{n,m} + \delta$ [44]

$$\begin{aligned} i\dot{A}_n + (\zeta_n + i\Gamma_n)A_n + \epsilon A_m^* &= \sqrt{2\Gamma_{n0}}B_n, \\ i\dot{A}_m + (\zeta_m + i\Gamma_m)A_m + \epsilon A_n^* &= \sqrt{2\Gamma_{m0}}B_m, \end{aligned} \tag{3.3}$$

where ζ_n and ζ_m are effective detunings equal to

$$\begin{aligned} \zeta_n &= \delta + \alpha_n|A_n|^2 + 2\alpha_g|A_m|^2, \\ \zeta_m &= \delta + \alpha_m|A_m|^2 + 2\alpha_g|A_n|^2. \end{aligned} \tag{3.4}$$

For simplicity, the geometric means of dampings $\Gamma = \sqrt{\Gamma_n\Gamma_m}$, and Duffing terms $\alpha_g = \sqrt{\alpha_n\alpha_m}$, are introduced. The second terms in Eq. (3.4) are again the Duffing or Kerr effects. Similarly, the third terms are equivalent to cross-Kerr effects. Both the Kerr and cross-Kerr lead to larger effective detunings ζ_n, resulting in lower resonant frequencies, as the intramode fields increase.

In the steady state, $\dot{A}_n = \dot{A}_m = 0$, and with no input fields, $B_n = B_m = 0$, Eq. (3.3) can be solved to produce the following expressions for the excited state intensities $|A_n|^2$ and $|A_m|^2$:

$$|A_n|^2 = \frac{2\Gamma_m(\delta_{\text{th}}(\epsilon) - \delta)}{R}, \quad |A_m|^2 = \frac{2\Gamma_n(\delta_{\text{th}}(\epsilon) - \delta)}{R}, \tag{3.5}$$

where R is a constant $R = \alpha_n\Gamma_m + \alpha_m\Gamma_n + 2\alpha_g(\Gamma_n + \Gamma_m)$, and the pump-dependent threshold detuning δ_{th} is given by

$$\delta_{\text{th}}(\epsilon) = \frac{\Gamma_n + \Gamma_m}{2}\sqrt{\frac{\epsilon^2}{\Gamma^2} - 1}. \tag{3.6}$$

The finite steady-state amplitudes is only stable for $\epsilon \geq \Gamma$ and $\delta \leq \delta_{\text{th}}$. The ground state $A_n = 0$ is stable for $\epsilon < \Gamma$ and $|\delta| > \delta_{\text{th}}$, thus three different regions exist in δ-ϵ space:

I. For $\epsilon < \Gamma$ or $\delta > \delta_{\text{th}}$ the ground states $A_n = A_m = 0$ is stable.

II. For $\epsilon \geq \Gamma$ and $|\delta| \leq \delta_{\text{th}}$ the excited states $|A_n|$ and $|A_m|$ are stable.

III. For $\epsilon \geq \Gamma$ and $\delta < -\delta_{\text{th}}$ both states are stable.

These are the same regions as for the degenerate case, see Fig. 3.1.

Where the phase of the degenerate parametric oscillations had a bi-stability, the nondegenerate parametric oscillations have a continuous degeneracy. The steady-state phases of the mode fields are denoted by θ_n and θ_m. Their sum is given by

$$\theta_n + \theta_m = \Theta \in \{\pi/2, \pi\}, \quad \tan\Theta = -1/\sqrt{\epsilon^2/\Gamma^2 - 1}, \tag{3.7}$$

while their difference $\theta_n - \theta_m$ is undefined. Therefore, the intermode phases have continuous degeneracies between $-\pi$ and π.

To study the effect of vacuum noise on the system, and more specifically its quantum properties such as entanglement, one would theoretically linearize around the classical solution and consider small deviations due to the noise. Here however, the large fluctuations in phase impose a problem as they are present already in the classical part, implying that it is not possible to linearize the model. Therefore, we are not able to perform any quantitative analysis of the noise in the quantum regime.

When solving for the steady state, another rotating frame is needed to obtain stationary solutions, namely $\omega_n + \delta + \Delta_0$ for mode n, and $\omega_m + \delta - \Delta_0$ for mode m, where

$$\Delta_0 = \frac{\Gamma_n \zeta_m - \Gamma_m \zeta_n}{\Gamma_n + \Gamma_m}. \tag{3.8}$$

This is in contrast to degenerate parametric oscillations where the oscillation is always at $\omega_n + \delta$, equal to half the pump frequency. The frequency shift is dependent on the asymmetry of the modes, *i.e.* , $\Gamma_n = \Gamma_m$ and $\alpha_n = \alpha_m$ would yield $\Delta_0 = 0$.

3.3 Measurement techniques

The cryogenic measurement setup is very similar to the one in Chapter 2. The main difference is at room temperature, where a vector digitizer detects the outgoing microwave signals. The digitizer downconverts the signal using heterodyne mixing to an IF frequency of 187.5 MHz, which is then sampled with an analog-to-digital converter (ADC) at 250 MS/s, illustrated in Fig. 3.2 (a). After digitization, an onboard FPGA filters and processes the signal by digital down conversion to zero frequency, as well as decimating it to an effective sampling frequency f_{s} [61]. It is important to choose the effective sampling rate high enough so all signals of interest are captured, but not much wider than that to minimize the amount of noise in the measurement. From the digitizer, the quadratures of the complex voltage, $I(t)$ and $Q(t)$, are transferred to a computer for further processing.

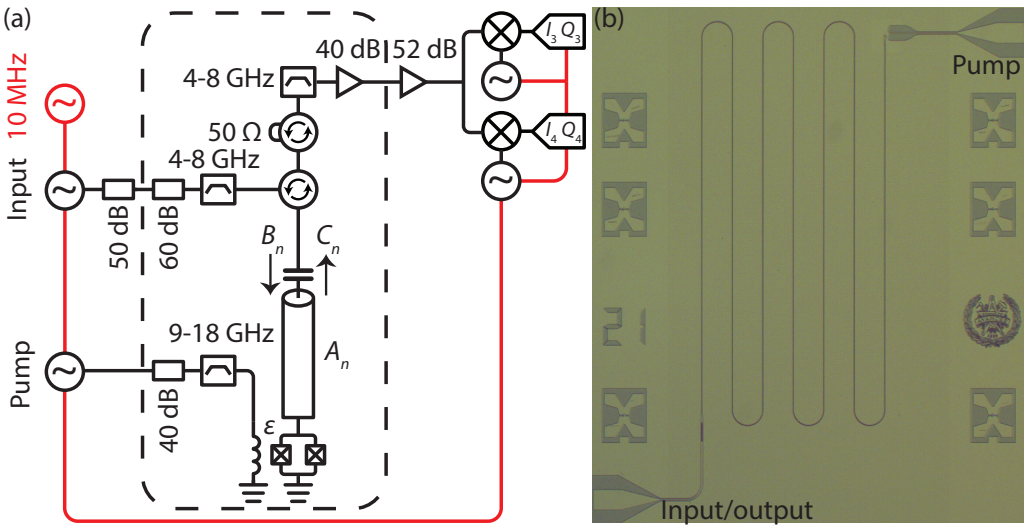

Figure 3.2: *(a) Measurement setup using a heterodyne detection scheme for detection of parametric oscillations. The outgoing signal is split to allow for detection at two frequencies far separated in frequency. The signals are then downconverted to an intermediate frequency using microwave mixers and signal generators. The downconverted signals are digitized with analog-to-digital converters (ADC). All signal generators and the ADCs are reference locked to the same 10 MHz signal (represented by the red lines) to ensure phase stability over time. (b) Micrograph of the device used to demonstrate nondegenerate parametric oscillations.*

The total power is calculated as $P = \langle I(t)^2 \rangle + \langle Q(t)^2 \rangle$, where the voltages are assumed to be over a $50\,\Omega$ resistor.

One complication when measuring power instead of amplitude is that the noise $X(t)$ doesn't average to zero, $\langle X(t) \rangle = 0 \implies \langle X(t)^2 \rangle = 0$. This implies that any measurement of the parametric-oscillation power will also include the power of the noise. However, by assuming that the noise is constant in time, the noise can be measured separately and subtracted from subsequent measurements. The measured output power can then be translated to output field intensity via $|C|^2 = (P - P_{\text{noise}})/G\hbar\omega_d$, where P_{noise} is the system noise power, G is the gain of the system, and ω_d is the detection frequency.

For simultaneous detection of two modes far separated in frequency, two vector digitizers are used. The digitizers uses two different, but phase locked, local oscillators. This ensures phase stability between the digitizers, which is important when correlating signals between the modes. One might ask, how can there even exist a phase relation between two signals with different frequencies? The answer is that the phase relation only exist under certain circumstances. One being when one frequency is a multiple of the other, or if the frequencies are connected to a third frequency which acts as a clock, *i.e.* $\omega_p = \omega_n + \omega_m$. It is also important to start the data acquisition for the digitizers simultaneously. This is achieved by a clock module, which distributes a common trigger signal to both digitizers in cables of equal length.

Due to the complexity of the measurements, such as the amount of data and instruments involved, computers are needed for synchronous hardware control and data logging. This work uses Labber$^{\text{TM}}$ for all instrument control, measurement automation, and data logging[1]. Each physical instrument has its own software instrument driver. The drivers are responsible from translating from a general command to a instrument specific command. For example, the user might request that the frequency of a signal generator to be set to 5 GHz. The driver then translates this to a command that the instrument understands. Most instruments are controlled via the standard commands for programmable instruments (SCPI) over either GPIB or Ethernet. Some instruments however, are mounted in a PXI rack requiring PCI communication. In general, these instruments do not follow the SCPI. Instead, they have their own dynamic-link libraries (DLL) for communication. For integration with Labber, a python wrapper is needed for each DLL. Most instrument drivers for both SCPI and PXI instruments are found on the Labber$^{\text{TM}}$ driver repository[2].

3.4 Gain and loss calibrations

A calibration of the system loss and gain is needed for proper measurements of the outgoing fields, as well as for calibration of the incoming fields. It is enough to know either the loss or the gain, since the other can be inferred by using that $|S_{11}| = 1$ far-off resonance. Subsequently, the number of photons inside the mode can be calculated using Eq. (3.2).

The gain is calibrated using a shot noise tunnel junction (SNTJ) [62, 63] connected to a microwave switch at the mixing chamber of the refrigerator. The SNTJ is a tunnel

[1] See http://labber.org for more information.
[2] See https://github.com/Labber-software/Drivers

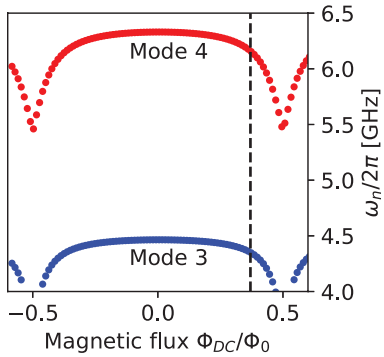

Figure 3.3: *Measured resonant frequencies for modes 3 and 4 as a function of magnetic flux through the SQUID loop. The vertical dashed line marks the static flux bias used in the reported experiments.*

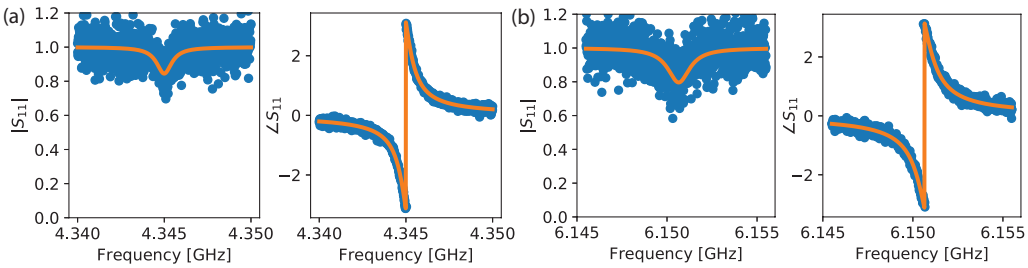

Figure 3.4: *Magnitude and phase of the complex reflection coefficients of modes 3 (a) and 4 (b). The solid lines are fits, which extract the resonant frequencies, and external and total loss rates. See the main text for the extracted parameters.*

junction made of a normal metal - insulator - normal metal. When a current is applied through the junction, shot noise is produced. The amount of shot noise depends on the resistance of the junction, and the current through the junction. Moreover, there is also thermal, vacuum, and amplifier noise. By measuring the total noise as a function of current through the junction, the contribution of the different noise processes can be extracted, together with the gain between the SNTJ and the detector. For practical reasons, the designed value of the SNTJ resistance is 50 Ω. For more information about the SNTJ and how it is used, see Ref. [64].

3.5 Demonstration of nondegenerate parametric oscillations

This section is a summary of the results of Paper A, where nondegenerate parametric oscillations in a superconducting microwave resonator were demonstrated using the device seen in 3.2 (b). Initially, the resonant frequencies are measured as a function of magnetic

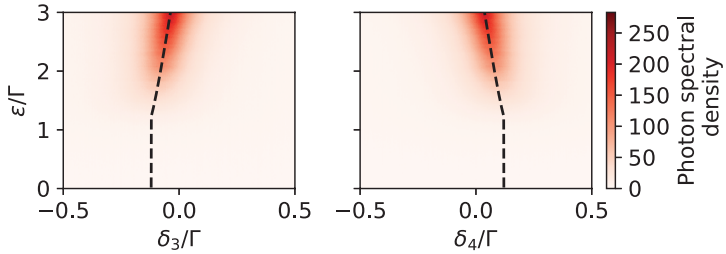

Figure 3.5: *Emergence of self-sustained parametric oscillations when increasing the pump amplitude. The detection frequency detunings δ_n from the rotating frame are shown on the x-axes. The pump detuning is fixed at $\delta = 0.26\Gamma$. The dashed lines are the resulting oscillation frequencies from the fit of Eq.* (3.8).

flux through the SQUID loop Φ_{DC}, see Fig. 3.3. A bias point with enough slope, but not too close to $\Phi_0/2$ is chosen. Close to $\Phi_0/2$ the nonlinearities α_n are large, and also the internal losses increase, and should therefore be avoided. The loss rates and the exact resonant frequencies of the two modes, $n = 3$ and $m = 4$, at the chosen bias point are determined by data fitting of the measured reflection coefficients to Eq. (2.20), see Fig. 3.4. At the static flux bias $\Phi_{\mathrm{DC}} = 0.37\Phi_0$ indicated in Fig. 3.3, $\omega_3/2\pi = 4.345\,\mathrm{GHz}$, $\omega_4/2\pi = 6.150\,\mathrm{GHz}$, $\Gamma_{30}/2\pi = 0.52\,\mathrm{MHz}$, $\Gamma_3/2\pi = 0.56\,\mathrm{MHz}$, $\Gamma_{40}/2\pi = 0.70\,\mathrm{MHz}$, and $\Gamma_4/2\pi = 0.78\,\mathrm{MHz}$.

To demonstrate nondegenerate parametric oscillations, a fixed pump detuning δ is used while increasing the pump amplitude ϵ. In Fig. 3.5 the observed output photon spectral density is plotted as a function of detuning δ_n from the rotating frame, $\delta_n = \omega_d - (\omega_n + \delta)$. The observed oscillations has some width corresponding to the frequency noise of the parametric oscillations. Also, the center frequency is changing with the pump amplitude. The center frequency for each pump amplitude is extracted and fitted to Eq. (3.8). The free parameters are α_3, α_4, and a conversion factor between the applied pump amplitude at the generator and the effective pump amplitude at the sample. The extracted nonlinearities are $\alpha_3/2\pi = 71\,\mathrm{kHz}$ and $\alpha_4/2\pi = 178\,\mathrm{kHz}$. One could instead use the observed oscillation intensities to extract α_n, however this method would suffer from systematic errors in the gain calibration, whereas the center-frequency extraction only has statistical errors that can be decreased by longer averaging.

Then, the output intensities $|C_n|^2$ are measured as a function of the pump detuning δ and amplitude ϵ, see Fig. 3.6(a-b). The oscillations start at a certain pump power, $\epsilon \approx \Gamma$, defining the instability threshold, and grows rapidly above that. The observed intensities can be compared with the theoretical steady-state amplitudes Eq. (3.5), see Fig. 3.6(c-d). We find good agreement inside regions I and II. However, in region III, where the ground and excited states are both stable, the discrepancy is larger. The model does not predict the probability of occupying the excited state; consequently Eq. (3.5) are the maximal achievable intensities. In the experiment, the resonator can switch between the two states, yielding a lower intensity on average. For large negative detunings, the observed probability for oscillations tends to zero. This is even more clear for line cuts of the four regions, see Fig. 3.6(e). There is excellent agreement in region II and all the

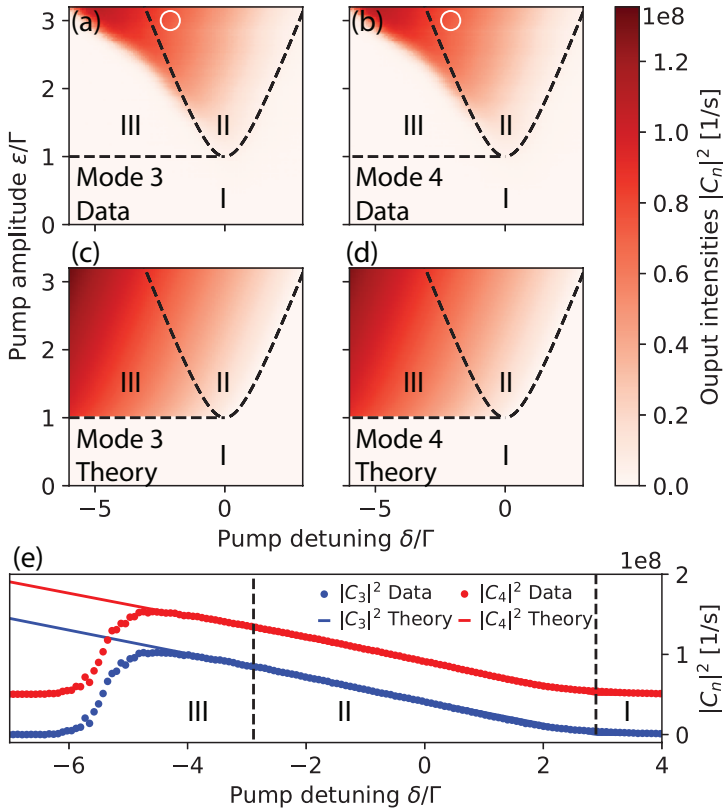

Figure 3.6: *Nondegenerate pumping of modes $n = 3$ and 4, at frequency $\omega_p = \omega_3 + \omega_4 + 2\delta$. (a-d) Experimentally observed and theoretical output intensities $|C_n|^2$ vs. detuning δ and amplitude ϵ of the applied pump tone. I-III indicate the three different stability regions described in the main text. (e) Horizontal line cuts of (a-d) at $\epsilon = 3\Gamma$. The red traces are offset for clarity.*

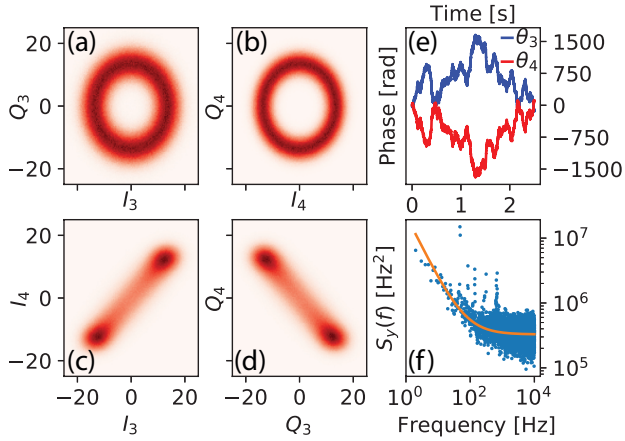

Figure 3.7: *Quadrature histograms of the nondegenerate parametric oscillations. Panels (a-b) show the phase-space distributions for the two modes measured at the point indicated by the white circles in Fig. 3.5. The color scale is proportional to the number of counts in each bin of the digitized output. (c-d) Two out of four cross-quadrature histograms. All histograms consist of 1 million samples each. (e) Evolution of the phases θ_n in time. (f) Frequency spectrum of the nondegenerate parametric oscillations in mode 3. The solid line is a combination of white and flicker noise.*

way down to $\delta \approx -4.5\Gamma$, implying that the system is mostly in the excited state. Below $\delta \approx -4.5\Gamma$ the excited state probability decreases rapidly.

To investigate the origin of the frequency noise shown in Fig. 3.5, we choose the point in δ-ϵ space indicated by the white circles in Fig. 3.6(a-b). We acquire quadrature voltages $I_n(t)$ and $Q_n(t)$, and calculate their phase-space distributions, see Fig. 3.7 (a-b). The oscillations have a finite average amplitude, while the phase is random, hence the large frequency noise.

To quantify if the observed state is quantum or classical, one would normally focus on the variances of the different quadratures. However, the large fluctuations in phase impose a problem as they introduce large variances of the individual quadratures. Also, theoretically it is a problem since a linearization around the classical solution is not possible for the same reason. Therefore, we are not able to perform any quantitative analysis of the possible quantum properties of the NJPO state.

However, we can study the cross-quadrature histograms I_3, I_4 and Q_3, Q_4 in Fig. 3.7 (c-d). From those histograms, it is clear that I_3 and I_4 have equal signs, while Q_3 and Q_4 have opposite signs, implying that the phase sum is fixed as predicted from Eq. (3.7).

The question is, what drives the phase evolutions? In Fig. 3.7(e) the phase evolution in time of the two modes are plotted, and the clear anti-correlation is observed. For illustration, the phases of the local oscillators are set so that $\langle \theta_3 + \theta_4 \rangle = 0$. From the phase evolution, the frequency noise spectrum $S_y(f)$ is extracted, see Fig. 3.7(f). The spectrum is a combination of $1/f$ and white noise. It is difficult to pinpoint the origin of the noise, but it is well known that SQUIDs have a $1/f$ flux noise spectrum [65]. Flux noise translates directly into frequency noise of the resonator, and therefore also into

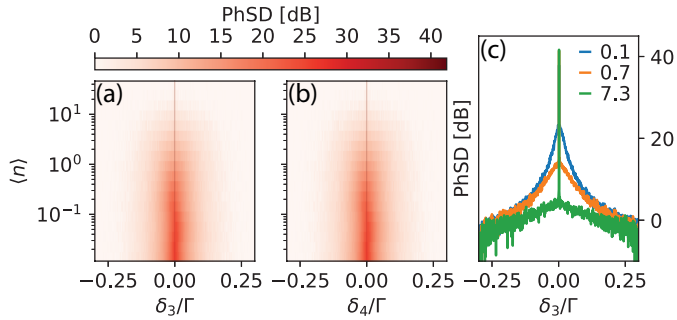

Figure 3.8: *Photon spectral densities (PhSD), in a logarithmic unit relative to 1 photon/sHz, under injection locking of a nondegenerate parametric oscillator. (a-b) PhSD for modes 3 (left) and 4 (right), in the presence of an injection signal in mode 3. The x-axes represent the detunings between the detection and the center of oscillation, and the y-axes represent the average number of injection photons in the mode. (c) Line cuts of (a) at the three photon numbers given in the legend.*

frequency noise of the parametric oscillations.

3.6 Injection locking

The frequency of an oscillator can be stabilized by injecting a small, but frequency stable, signal on-resonance with the oscillator [66], which has been utilized in a variety of systems [67–70]. We apply the same technique here by injecting a coherent signal B_3 on resonance with the parametric oscillations in mode 3. The input field generates an average number of coherent photons in the mode of $\langle n \rangle = |B_3|^2 2\Gamma_{30}/\Gamma_3^2$.

The injection locking lifts the phase degeneracy of the phase variables and leads to narrower photon spectral densities, see Fig. 3.8(a-b). In Fig. 3.8(c) we plot line cuts for three different injection powers. For 0.1 photons the oscillation is still wide, but when the input power is increased to 0.7 photons the width is strongly reduced, and for 7.3 photons the frequency noise is removed almost entirely. The -3 dB point is below the resolution bandwidth of 1 Hz, implying a frequency-noise reduction of at least a factor 5000.

4

Single-shot readout of a superconducting qubit

Superconducting quantum bits (qubits) have had a tremendous development since the first demonstration in 1999 [71]. Their coherence times, the gate and readout fidelities, and the number of coupled qubits have all improved with orders of magnitudes. However, there is still a long way to go before a large-scale universal quantum computer can be demonstrated. The largest improvement has been in the coherence time, which is now in the 100 µs range, compared to a few nanoseconds in the first qubit. With that problem under control for now, the focus have shifted to scaling up the systems from just a few qubits to tens of qubits. A great challenge is to maintain the long coherence times while scaling due to the complex 3D geometries needed [72].

Even if both the readout and the gate fidelities now exceed 99 %, they are still a bottleneck for running long quantum algorithms with active feedback [73]. This chapter is focused on the problem of reading out the qubit's state with high fidelity which is normally done with a parametric amplifier. Here, we omit the parametric amplifier, and implement a high fidelity readout using a Josephson parametric oscillator.

There are many different types of superconducting qubits [74]. Almost all superconducting qubits have in common that their transition frequencies are in the GHz regime and that they utilize the Josephson nonlinearity in some way. One of the most popular qubits is the transmon [75], which is a capacitively shunted Josephson junction. The transmon is modeled as a highly nonlinear LC resonator. Since the inductance of the Josephson junction is nonlinear, it leads to anharmonicity in the spectrum of the LC circuit. If the anharmonicity is large enough, the two lowest energy levels of the oscillator, denoted $|0\rangle$ and $|1\rangle$, can be isolated and used as a qubit, see Fig. 4.1 (b). For the transmon, the anharmonicity is usually around 5 % of the transition frequency.

In the circuit quantum electrodynamic (cQED) architecture [21], a qubit is strongly coupled to a resonator [76]. It allows for fast and accurate state readout, qubit-qubit coupling, gives protection from the environment, and much more. A two-level system (qubit) coupled to an harmonic oscillator (microwave resonator) is typically described by

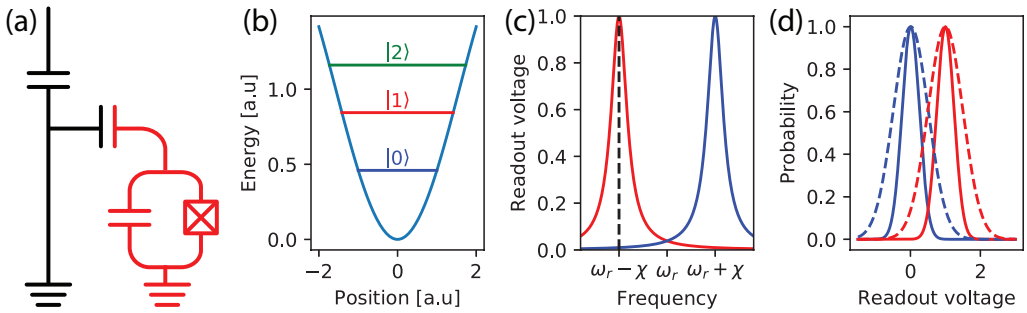

Figure 4.1: *(a) Transmon qubit (red) coupled to a microwave resonator (black). (b) Illustration of the transmon spectrum including the three lowest energy levels. Note that the distance between* $|1\rangle$ *and* $|2\rangle$ *is smaller than the distance between* $|0\rangle$ *and* $|1\rangle$*. (c) Readout voltage as a function of frequency. The dispersive shift* χ *moves the resonant frequency dependent on the qubit's state. (d) Normal distributions of the readout voltage when applied at the dashed black line in (c), dependent on the qubit's state. The dashed lines have twice the width of the solid lines, illustrating a larger overlap of the Gaussians, and therefore a lower readout fidelity.*

the Jaynes-Cummings Hamiltonian, which after a rotating-wave approximation equals to [9]

$$\hat{H}/\hbar = \omega_r\left(\hat{a}^\dagger\hat{a} + \frac{1}{2}\right) + \frac{\omega_a}{2}\hat{\sigma}_z + g\left(\hat{\sigma}_+\hat{a} + \hat{\sigma}_-\hat{a}^\dagger\right), \tag{4.1}$$

where $\hat{a}$ is the annihilation operator for the harmonic oscillator, $\sigma_\pm$ are the raising and lowering operators for the qubit, g is the coupling strength, and ω_r and ω_a are the frequencies of the harmonic oscillator and qubit, respectively.

However, Eq. (4.1) is not enough to describe the full behavior of an implementation of a qubit. The environment is interacting with the qubit, causing for example relaxation back into the ground state or thermal excitation to higher levels. It is difficult to model the microscopics of the environment due to the many degrees of freedom involved. Instead, statistical properties of the qubit-environment interaction are used. These include the qubit's effective temperature T, and relaxation time T_1. If the qubit is initialized to its excited state, it will relax back into its ground state with the characteristic time scale T_1, which is defined as the time where the probability of finding the qubit in its excited state is equal to $1/e$, in the case of an exponential decay.

4.1 Qubit control and readout

For qubits to have an advantage over classical bits, the qubits need to be put into coherent superpositions and entangled with each other. To produce an arbitrary single-qubit state $c_0\,|0\rangle + c_1\,|1\rangle$, a sinusoidal drive at the qubit frequency can be used. The amplitude, phase, and length of the drive determine the complex coefficients c_0 and c_1 [77]. For proper normalization, $|c_0|^2 + |c_1|^2 = 1$ is required. The qubit's state can be represented by the position on a (Bloch) sphere where $|0\rangle$ is on one pole and $|1\rangle$ on the other. The control pulse that transfers the qubit from one pole to the other is called a π pulse since it rotates

the state by π radians. There is a subfield of the circuit-QED community that focuses on optimal control of qubits, see for example Ref. [78].

For measurement of the qubit's state, the dispersive coupling regime is typically used. This regime is valid when $|\Delta| \gg g$, where $\Delta = \omega_a - \omega_r$ is the qubit-resonator detuning. In this limit the Jaynes-Cummings Hamiltonian can be rewritten as

$$\hat{H}_{\text{disp}}/\hbar = \left(\omega_r + \frac{g^2}{\Delta}\hat{\sigma}_z\right)\hat{a}^\dagger\hat{a} + \frac{1}{2}\left(\omega_a + \frac{g^2}{\Delta}\right)\hat{\sigma}_z. \tag{4.2}$$

As a result of the dispersive coupling, the effective resonator frequency is $\omega_r + \frac{g^2}{\Delta}\hat{\sigma}_z = \omega_r + \chi\hat{\sigma}_z$, where $\chi = g^2/\Delta$ is the dispersive shift, meaning that the resonator frequency is dependent on the qubit's state, see Fig. 4.1 (c). This allows the state of the qubit to be inferred by measuring the resonant frequency of the resonator. Experimentally, a single microwave tone is applied at one frequency, and the reflected signal is measured. Depending on where the resonant frequency is, the readout voltage will be different, and the qubit's state can be inferred.

Accurate readout is made difficult due to noise. The readout voltage will have a Gaussian distribution, whose width is given by the total system noise, see Fig. 4.1 (d). The readout fidelity F is defined via the overlap between the measurement distributions with the qubit in the ground respective excited state. This overlap equals to $1 - F$. A signal-to-noise ratio, SNR, can also be defined as $\text{SNR} = \left|\mu_{|1\rangle} - \mu_{|0\rangle}\right|/(\sigma_{|1\rangle} + \sigma_{|0\rangle})$, where μ and σ are the mean and standard deviation for the respective states.

Ideally, the only contribution to the noise would be from the vacuum. However, in most practical applications, the semiconducting amplifier used adds noise which dominates over the vacuum. This causes an overlap between the readout voltage distributions corresponding to the qubit in the ground and the excited state, yielding a lower readout fidelity, see the dashed lines in Fig. 4.1 (d).

To mitigate this, two methods could be used. Either the Gaussian's width (noise) is reduced, or the separation (signal) is increased. To reduce the noise, several different techniques have been developed over the years. Most of them rely on some parametric phenomena to achieve vacuum-noise limited amplification. For example, a Josephson parametric amplifier was used as the first-stage amplifier to demonstrate single-shot readout [79, 80].

Normally, the SNR can be increased by just increasing the signal, which is the amplitude of the microwave tone used for readout. However, if the amplitude is too large, the approximations done to the dispersive Hamiltonian Eq. (4.2) breaks down and the resonant frequency is no longer dependent on the qubit's state [9]. Unfortunately, it turns out that the critical number of photons in the readout signal is just a few photons for normal experimental parameters, which is lower than the number of noise photons added by the best available semiconducting amplifiers.

However, a non-linear detector could be used to increase the signal. In this case, a small change in the resonant frequency yields a large readout signal [81–83]. The drawback of a large readout signal is that it takes time for the resonator to relax back into its ground state. Also, a high photon population of the resonator can cause dephasing of the qubit [84], which is a source of decoherence.

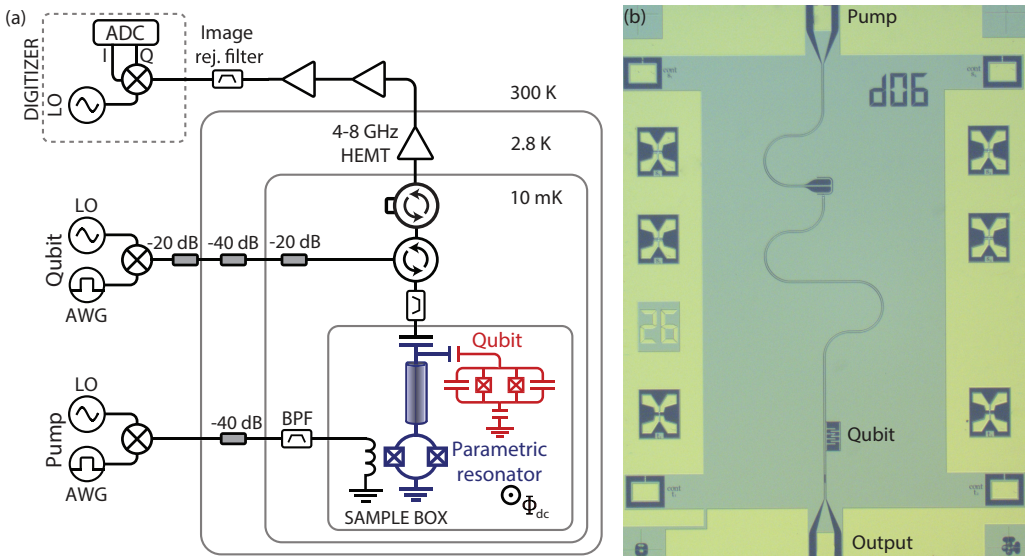

Figure 4.2: *(a) Experimental setup for the Josephson parametric readout. A transmon qubit (red) is coupled to a Josephson parametric oscillator (blue). Both the qubit control and the readout parametric pump is controlled by a microwave mixer and an arbitrary waveform generator. The outgoing field is amplified and detected using heterodyne mixing. (b) Micrograph of a similar device to the one used in Paper B.*

4.2 Readout using a Josephson parametric oscillator

The excitation of oscillations in a Josephson parametric oscillator (JPO) is sensitive to the pump conditions. The pump amplitude must exceed the instability threshold, and the frequency must be close to $2\omega_r$. By coupling a superconducting qubit, such as the transmon, to the JPO, see Fig. 4.2, the dispersive shift can move the resonant frequency so that the second criterion is no longer fulfilled. The JPO will then remain in its ground state. In this way, the ground state of the qubit can be mapped to an oscillating JPO, and the excited state to a silent JPO, or *vice versa*. Since the oscillating state has a large number of photons in the resonator, there will be a large measurement contrast between the outputs corresponding to the two qubit states, and therefore an improved signal-to-noise ratio. This was proposed in Ref. [42] and demonstrated in Paper B.

For controlling and reading out the qubit, both the parametric pump and the qubit control need to be pulsed in a controlled way. This is achieved by combining microwave signal generators, mixers, and an arbitrary waveform generator (AWG). The mixer acts as a valve for the microwave signal, and the valve is controlled by the AWG.

The detection of the response to the parametric pump is done using heterodyne mixing as in Chapter 3. However, proper triggering of the ADC is now important since the parametric pump is pulsed. A trigger is sent from the AWG to the ADC at the start of the pump pulse. The ADC then acquires the quadrature voltages for a certain time and integrates over this time window. The pulse sequence is repeated to build statistics of

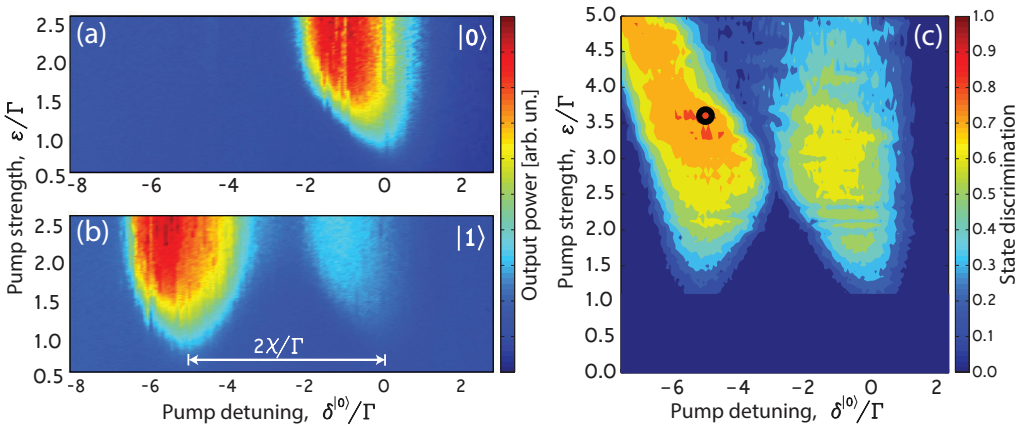

Figure 4.3: *Measurements of the output power of the parametric oscillations as a function of the pump parameters, when the qubit is prepared in the ground state (a) and excited state (b). (c) Readout fidelity as a function of the pump parameters.*

the readout voltage. Note that it is not allowed to average over several pulses, since this is supposed to be a single-shot measurement. For more details about the experimental details of the parametric qubit readout, see Ref. [47].

In Fig. 4.3 (a) and (b), the output power of the JPO is presented as a function of the pump detuning and amplitude, when the qubit is prepared in the ground and excited states, respectively. For the ground state, a normal parametric region is seen. For the excited state the region has moved to lower frequencies due to the dispersive shift χ. However, a faint region is still seen at the original position. This is due to qubit relaxation back to its ground state before the readout, or that the excitation pulse was not successful.

It is clear that if the JPO is operated close to zero detuning the finite-amplitude state is mapped to $|0\rangle$ and the zero-amplitude state to $|1\rangle$. However, if operated at negative detunings the situation is reversed. The optimal operating point is found by extracting the maximum fidelity at each point in the parametric regions, see Fig. 4.3 (c). The maximum fidelity is given by calculating the maximum difference between the cumulative distributions functions for the readout voltage with the qubit prepared in its ground, respective, excited state.

For the operating point with the highest readout fidelity, 81.5%, the readout voltage distributions are analyzed in detail in Fig. 4.4. With the qubit in the ground state, the oscillator is in its zero amplitude state (one Gaussian at the origin), while in the excited state the oscillator has a finite amplitude. Moreover, it shows a combination of three Gaussians. The two outer ones are brighter, meaning that these are the preferred states. The reason for two peaks at finite voltages is that the JPO has two degenerate states, shifted by π radians. The central peak is due to errors in the readout and will be explained later.

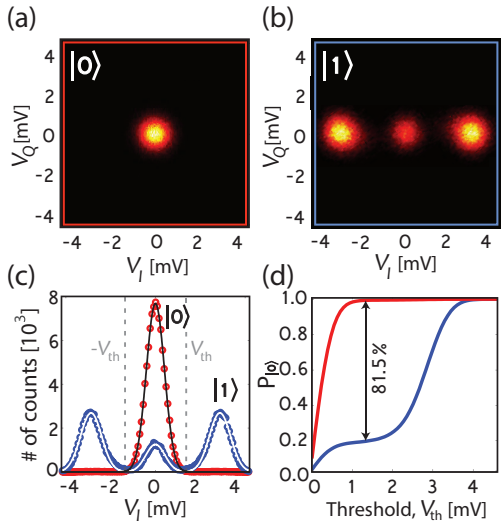

Figure 4.4: *Quadrature histograms of the parametric oscillations at the point indicated in Fig. 4.3 (c). (a) and (b) correspond to the qubit prepared in its ground and excited state, respectively. (c) Histogram of only the I quadrature. The solid lines are Gaussian fits. (d) Cumulative distribution functions for the respective state preparation. The separation of the curves equals the readout fidelity, and the maximum separation is indicated.*

4.3 Modeling of the readout fidelity

Performing a carful analysis of the acquired histograms can give insights to the origins of the fidelity loss. Ideally, the distribution for each state should be Gaussian. However, the distributions experimentally deviate from Gaussians, see Fig. 4.4 (c). For example, when the qubit relaxes before the start of the readout, the excited state measurement shows three Gaussians instead of two. If the qubit instead relaxes during the readout, it introduces an asymmetry in the Gaussians.

Due to the probabilistic nature of the effects limiting the readout fidelity, we use a Monte-Carlo based simulation of the experiment. The simulation starts with the qubit initialized to its ground state, then several random numbers between 0 and 1 are generated and compared to the probability of certain processes, deciding if that processes will happen during one cycle of the experiment. The final qubit state is recorded and a readout voltage is drawn from the associated Gaussian distribution. The simulation is then repeated, but with different random numbers. Over time, a distribution of qubit states and readout voltages are built up.

There are five sources of error taken into account in the simulation

1. Qubit is not in its ground state initially. This probability is given by the Boltzmann distribution for a certain qubit frequency and temperature.

2. Qubit is not excited by the π pulse, which is modeled as a gate fidelity.

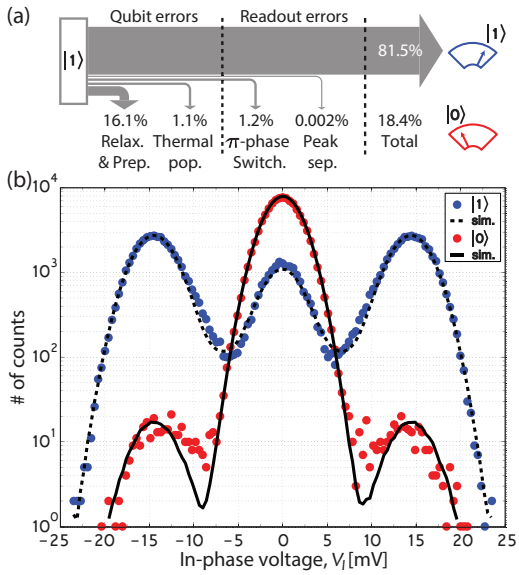

Figure 4.5: *Analysis of the factors contributing to a decreased readout fidelity. (b) I-quadrature histogram with a logarithmic y scale, together with the simulation results.*

3. Qubit relaxes before readout. The probability of decay after a given delay time t_d between the excitation pulse and the start of the readout is given by $1 - e^{-t_d/T_1}$.

4. Qubit relaxes during readout. The probability of decay in a given time interval Δt is given by $e^{-\Delta t/T_1}\Delta t/T_1$.

5. Parametric oscillator switches during readout. The probability is given by the switching rate.

The probability of switching, and the relaxation time T_1 are measured separately, while the gate fidelity and the temperature of the qubit are treated as fitting parameters.

In Fig. 4.5 (b) the result of the simulation and the experimental data is compared. The side peaks in the red data set corresponds to the qubit initially being in the excited state due to thermal excitation. The temperature in the simulation is therefore adjusted accordingly. Moreover, the central peak in the blue data set corresponds to either relaxation before the readout, an unsuccessful π pulse, or the qubit being in the excited state initially and then de-excited by the π pulse. Since T_1 is measured separately and T is already fixed, only the gate fidelity is adjusted in the simulation. These two adjustments gives an overall good agreement with experimental data and simulation. The loss of fidelity associated with each error channel is summarized in Fig. 4.5 (a). From this analysis we draw the conclusion that the fidelity due to the readout method itself is 98.7%.

There are a few things that could be done to improve the fidelity. The main loss of fidelity is the switching between the two π-shifted states of the JPO. What determines the switching rate is still unknown to a large extent, but two things could be done to

improve it. Either, the readout duration is decreased so that the probability of switching during the readout is lower, or the oscillations can be injection locked to one of the states by applying a small signal on-resonance, as done in Ref. [83].

The qubit induced readout errors are mainly due to the low coherence time compared to the readout duration. Modern qubits have coherence times at least 10 times longer than the one used here, and should therefore reduce errors 3 and 4 substantially. The gate fidelity could also be improved by a more systematic calibration of the qubit excitation pulse [85], and by using a better shape of the pulse [78].

5

Summary and outlook

In summary, this work has revolved around the Josephson parametric oscillator (JPO), which is based on a frequency tunable microwave resonator. After some introductory theory and descriptions of superconducting circuits, we outlined the field amplitude formalism for degenerate and nondegenerate parametric oscillations in a tunable resonator.

In Paper A, we demonstrated the nondegenerate Josephson parametric oscillator (NJPO) regime in a multimode microwave resonator. The NJPO was realized by pumping at the sum of two resonant frequencies with an amplitude larger than an instability threshold. We investigated the classical properties of the NJPO, such as the output intensities as a function of the pump parameters. We observed that the sum of the intermode phases was fixed, but the difference was not, leading to a continuous degeneracy of the intramode phases. Furthermore, by injecting a small coherent signal on-resonance with the parametric oscillations in one of the modes, we phase locked the oscillations and reduced the frequency noise with at least a factor 5000.

It has been theoretically proposed that the NJPO could exhibit novel quantum states useful for quantum information processing applications. However, before the NJPO can be used in such applications, more theoretical work is needed on how to characterize the NJPO states in presence of the large fluctuations, together with experimental methods of quantifying these fluctuations and the NJPO state. The noisy amplifiers used, and the lack of microwave single photon detectors, provide great challenges on the experimental part of that work.

In Paper B, we utilized a JPO in the cQED architecture to read out the state of a superconducting transmon qubit with high fidelity, without the need of a quantum limited parametric amplifier. By carful analysis of different sources of fidelity loss, we could show that the fidelity of the readout itself was 98.7 %. Since that work was performed, new and better parametric amplifiers have been developed which allows for single-shot readout using the normal dispersive readout. The saturation power and bandwidths of these amplifiers are now sufficiently high so that multiple qubits can be read out simultaneously. Therefore, it is not obvious that the method presented here is so advantageous as it once was. The cQED field is constantly developing new methods, so that all the criteria for building a large scale quantum computer is met.

Appendix A

Fabrication of tunable resonators

Cleaning of silicon

- Acetone for 5 min in ultrasonic
- Methanol for 5 min in ultrasonic
- IPA for 5 min in ultrasonic
- Blow dry with N_2
- Dip in 2% HF for 30 sec
- Quick dump rinse (QDR)
- Blow dry with N_2

Deposition of niobium

- Pre-sputter for 5 min
- Sputter for 2 min with 200 W, 8 µbar and 60 sccm of argon

Patterning and etching of niobium resonators

- 1165 Remover at 70°C for 5 min
- Rinse in IPA
- Blow dry with N_2

- Ash in oxygen plasma, 50W for 20 sec
- Pre-bake at 115°C for 1 min
- Spin S1805 at 3000 rpm for 1 min
- Soft-bake at 115°C for 2 min
- Expose in DWL. Intensity 80, Focus 5, Transmission 100
- Develop using MF319 for 45 sec
- Ash in oxygen plasma, 50W for 20 sec
- Etching using 50 sccm of NF_3, RF 30 W, ICP 200 W
- Ash in oxygen plasma, 50W for 30 sec

Patterning of SQUIDs

- 1165 Remover at 70°C for 5 min
- Rinse in IPA
- Blow dry with N_2
- Ash in oxygen plasma, 50W for 20 sec
- Pre-bake at 170°C for 1 min
- Spin MMA(8.5)EL10 500 rpm for 5 sec, 2000 rpm for 45 sec
- Soft-bake at 170°C for 5 min
- Spin ARP 3200.09 2:1 3000 rpm for 1 min
- Soft-bake at 170°C for 5 min
- Expose with 2 nA with a dose of 280 $\mu C/mm^2$
- Dice into 24 samples

Deposition of SQUIDs

- Develop top layer using n-Amylacetate for 2 min
- Rinse in IPA
- Blow dry with N_2
- Develop bottom layer using H_2O:IPA 1:4 for 7 min

- Rinse in IPA
- Blow dry with N_2
- Ash in oxygen plasma, 50W for 20 sec
- Argon ion milling, 250V, 20mA, $\pm 30°$, 1+1 min
- Evaporate 40 nm aluminum from $25°$
- Oxidize with a pressure of 0.2 mBar for 30 min
- Evaporate 65 nm aluminum from $-25°$
- Lift-off in 1165 Remover at 70°C
- Rinse in IPA
- Blow dry with N_2

References

[1] A. Bengtsson, P. Krantz, M. Simoen, I. M. Svensson, B. H. Schneider, V. Shumeiko, P. Delsing, and J. Bylander. Nondegenerate parametric oscillations in a tunable superconducting resonator. *To be submitted to Physical Review B.*

[2] P. Krantz, A. Bengtsson, M. Simoen, S. Gustavsson, V. Shumeiko, W. Oliver, C. Wilson, P. Delsing, and J. Bylander. Single-shot read-out of a superconducting qubit using a Josephson parametric oscillator. *Nature Communications* **7**, 2016.

[3] S. R. Sathyamoorthy, A. Bengtsson, S. Bens, M. Simoen, P. Delsing, and G. Johansson. Simple, robust, and on-demand generation of single and correlated photons. *Physical Review A* **93**: 063823, 2016.

[4] I. M. Svensson, M. Pierre, W. Wustmann, P. Krantz, A. Bengtsson, G. Johansson, J. Bylander, V. Shumeiko, and P. Delsing. Microwave photon generation in a doubly tunable superconducting resonator. *To be published in Journal of Physics: Conference Series.*

[5] I.-M. Svensson, A. Bengtsson, P. Krantz, J. Bylander, V. Shumeiko, and P. Delsing. Period-tripling subharmonic oscillations in a driven superconducting resonator. *Physical Review B* **96**: 174503, 2017.

[6] J. Burnett, A. Bengtsson, D. Niepce, and J. Bylander. Noise and loss of superconducting aluminium resonators at single photon energies. *To be published in Journal of Physics: Conference Series.*

[7] M. Tinkham. *Introduction to superconductivity.* Courier Corporation, 2012.

[8] T. Van Duzer and C. W. Turner. *Principles of superconductive devices and circuits.* Edward Arnold, 1981.

[9] A. Blais, R.-S. Huang, A. Wallraff, S. M. Girvin, and R. J. Schoelkopf. Cavity quantum electrodynamics for superconducting electrical circuits: An architecture for quantum computation. *Physical Review A* **69**: 062320, 2004.

[10] R. H. Hadfield and G. Johansson. *Superconducting Devices in Quantum Optics.* Springer, 2016.

[11] J. Clarke and A. I. Braginski. *The SQUID handbook.* Wiley Online Library, 2006.

[12] M. Sandberg, C. M. Wilson, F. Persson, T. Bauch, G. Johansson, V. Shumeiko, T. Duty, and P. Delsing. Tuning the field in a microwave resonator faster than the photon lifetime. *Applied Physics Letters* **92**: 203501, 2008.

[13] Y. Yin, Y. Chen, D. Sank, P. O'Malley, T. White, R. Barends, J. Kelly, E. Lucero, M. Mariantoni, A. Megrant, C. Neill, A. Vainsencher, J. Wenner, A. N. Korotkov,

A. N. Cleland, and J. M. Martinis. Catch and release of microwave photon states. *Physical Review Letters* **110**: 107001, 2013.

[14] T. Yamamoto, K. Inomata, M. Watanabe, K. Matsuba, T. Miyazaki, W. D. Oliver, Y. Nakamura, and J. S. Tsai. Flux-driven Josephson parametric amplifier. *Applied Physics Letters* **93**: 042510, 2008.

[15] E. Zakka-Bajjani, F. Nguyen, M. Lee, L. R. Vale, R. W. Simmonds, and J. Aumentado. Quantum superposition of a single microwave photon in two different colour states. *Nature Physics* **7**: 599–603, 2011.

[16] R. Z. Sagdeev, D. Usikov, and G. M. Zaslavskii. *Nonlinear physics: from the pendulum to turbulence and chaos*. Harwood Academic, 1990.

[17] S. H. Strogatz. *Nonlinear dynamics and chaos: with applications to physics, biology, chemistry, and engineering*. Hachette UK, 2014.

[18] J. A. Giordmaine and R. C. Miller. Tunable coherent parametric oscillation in $LiNbO_3$ at optical frequencies. *Physical Review Letters* **14**: 973, 1965.

[19] C. Wilson, T. Duty, M. Sandberg, F. Persson, V. Shumeiko, and P. Delsing. Photon generation in an electromagnetic cavity with a time-dependent boundary. *Physical Review Letters* **105**: 233907, 2010.

[20] R. J. Schoelkopf and S. M. Girvin. Wiring up quantum systems. *Nature* **451**: 664–669, 2008.

[21] M. H. Devoret and R. J. Schoelkopf. Superconducting circuits for quantum information: an outlook. *Science* **339**: 1169–1174, 2013.

[22] M. A. Nielsen and I. Chuang. *Quantum computation and quantum information*. AAPT, 2002.

[23] D. P. DiVincenzo. Quantum computation. *Science* **270**: 255–261, 1995.

[24] V. B. Braginsky, Y. I. Vorontsov, and K. S. Thorne. Quantum nondemolition measurements. *Science* **209**: 547–557, 1980.

[25] S. L. Braunstein and P. Van Loock. Quantum information with continuous variables. *Reviews of Modern Physics* **77**: 513, 2005.

[26] M. Hofheinz, H. Wang, M. Ansmann, R. C. Bialczak, E. Lucero, M. Neeley, A. D. O'connell, D. Sank, J. Wenner, J. M. Martinis, and A. N. Cleland. Synthesizing arbitrary quantum states in a superconducting resonator. *Nature* **459**: 546–549, 2009.

[27] C. Eichler, D. Bozyigit, C. Lang, M. Baur, L. Steffen, J. M. Fink, S. Filipp, and A. Wallraff. Observation of two-mode squeezing in the microwave frequency domain. *Physical Review Letters* **107**: 113601, 2011.

[28] E. Flurin, N. Roch, F. Mallet, M. H. Devoret, and B. Huard. Generating entangled microwave radiation over two transmission lines. *Physical Review Letters* **109**: 183901, 2012.

[29] C. W. Chang, M. Simoen, J. Aumentado, C. Sabín, P. Forn-Díaz, A. Vadiraj, F. Quijandría, G. Johansson, I. Fuentes, and C. M. Wilson. Generating Multimode Entangled Microwaves with a Superconducting Parametric Cavity. *arXiv preprint arXiv:1709.00083*, 2017.

[30] B. Vlastakis, G. Kirchmair, Z. Leghtas, S. E. Nigg, L. Frunzio, S. M. Girvin, M. Mirrahimi, M. H. Devoret, and R. J. Schoelkopf. Deterministically encoding quantum information using 100-photon Schrödinger cat states. *Science* **342**: 607–610, 2013.

[31] K. V. Kheruntsyan and K. G. Petrosyan. Exact steady-state Wigner function for a nondegenerate parametric oscillator. *Physical Review A* **62**: 015801, 2000.

[32] N. C. Menicucci, P. van Loock, M. Gu, C. Weedbrook, T. C. Ralph, and M. A. Nielsen. Universal quantum computation with continuous-variable cluster states. *Physical review letters* **97**: 110501, 2006.

[33] D. M. Pozar. *Microwave engineering*. John Wiley & Sons, 2009.

[34] H. Padamsee. The science and technology of superconducting cavities for accelerators. *Superconductor science and technology* **14**: R28, 2001.

[35] J. Baselmans. Kinetic inductance detectors. *Journal of Low Temperature Physics* **167**: 292–304, 2012.

[36] R. Loudon. *The quantum theory of light*. OUP Oxford, 2000.

[37] C. P. Wen. Coplanar waveguide: A surface strip transmission line suitable for nonreciprocal gyromagnetic device applications. *Microwave Theory and Techniques, IEEE Transactions on* **17**: 1087–1090, 1969.

[38] B. A. Mazin. *Microwave kinetic inductance detectors*. PhD thesis. California Institute of Technology, 2005.

[39] R. Barends. *Photon-detecting superconducting resonators*. PhD thesis. Delft University of Technology, 2009.

[40] D. T. Sank. *Fast, accurate state measurement in superconducting qubits*. PhD thesis. University of California, Santa Barbara, 2014.

[41] M. Wallquist, V. Shumeiko, and G. Wendin. Selective coupling of superconducting charge qubits mediated by a tunable stripline cavity. *Physical Review B* **74**: 224506, 2006.

[42] W. Wustmann and V. Shumeiko. Parametric resonance in tunable superconducting cavities. *Physical Review B* **87**: 184501, 2013.

[43] M. Simoen, C. Chang, P. Krantz, J. Bylander, W. Wustmann, V. Shumeiko, P. Delsing, and C. Wilson. Characterization of a multimode coplanar waveguide parametric amplifier. *Journal of Applied Physics* **118**: 154501, 2015.

[44] W. Wustmann and V. Shumeiko. Nondegenerate Parametric Resonance in a Tunable Superconducting Cavity. *Physical Review Applied* **8**: 024018, 2017.

[45] J. M. Sage, V. Bolkhovsky, W. D. Oliver, B. Turek, and P. B. Welander. Study of loss in superconducting coplanar waveguide resonators. *Journal of Applied Physics* **109**: 063915, 2011.

[46] C. Wang, C. Axline, Y. Y. Gao, T. Brecht, Y. Chu, L. Frunzio, M. H. Devoret, and R. J. Schoelkopf. Surface participation and dielectric loss in superconducting qubits. *Applied Physics Letters* **107**: 162601, 2015.

[47] P. Krantz. *The Josephson parametric oscillator-From microscopic studies to single-shot qubit readout*. PhD thesis. Chalmers University of Technology, 2016.

[48] C. Müller, J. H. Cole, and J. Lisenfeld. Towards understanding two-level-systems in amorphous solids-Insights from quantum devices. *arXiv preprint arXiv:1705.01108*, 2017.

[49] A. Bruno, G. De Lange, S. Asaad, K. Van der Enden, N. Langford, and L. DiCarlo. Reducing intrinsic loss in superconducting resonators by surface treatment and deep etching of silicon substrates. *Applied Physics Letters* **106**: 182601, 2015.

[50] A. T. A. M. de Waele. Basic Operation of Cryocoolers and Related Thermal Machines. *Journal of Low Temperature Physics* **164**: 179–236, 2011.

[51] I. Nsanzineza and B. L. T. Plourde. Trapping a Single Vortex and Reducing Quasiparticles in a Superconducting Resonator. *Phys. Rev. Lett.* **113**: 117002, 2014.

[52] G. K. White and P. Meeson. *Experimental Techniques in Low-Temperature Physics*. 4th ed. OUP Oxford, 2002, pp. 153–164.

[53] A. Heidmann, R. J. Horowicz, S. Reynaud, E. Giacobino, C. Fabre, and G. Camy. Observation of quantum noise reduction on twin laser beams. *Physical Review Letters* **59**: 2555, 1987.

[54] A. S. Villar, L. S. Cruz, K. N. Cassemiro, M. Martinelli, and P. Nussenzveig. Generation of bright two-color continuous variable entanglement. *Physical Review Letters* **95**: 243603, 2005.

[55] A. S. Coelho, F. A. S. Barbosa, K. N. Cassemiro, A. S. Villar, M. Martinelli, and P. Nussenzveig. Three-color entanglement. *Science* **326**: 823–826, 2009.

[56] B. Yurke, L. R. Corruccini, P. G. Kaminsky, L. W. Rupp, A. D. Smith, A. H. Silver, R. W. Simon, and E. Whittaker. Observation of parametric amplification and deamplification in a Josephson parametric amplifier. *Physical Review A* **39**: 2519, 1989.

[57] N. Roch, E. Flurin, F. Nguyen, P. Morfin, P. Campagne-Ibarcq, M. H. Devoret, and B. Huard. Widely tunable, nondegenerate three-wave mixing microwave device operating near the quantum limit. *Physical Review Letters* **108**: 147701, 2012.

[58] M. I. Dykman, C. M. Maloney, V. Smelyanskiy, and M. Silverstein. Fluctuational phase-flip transitions in parametrically driven oscillators. *Physical Review E* **57**: 5202, 1998.

[59] S. Puri, S. Boutin, and A. Blais. Engineering the quantum states of light in a Kerr-nonlinear resonator by two-photon driving. *npj Quantum Information* **3**: 18, 2017.

[60] M. Mirrahimi, Z. Leghtas, V. V. Albert, S. Touzard, R. J. Schoelkopf, L. Jiang, and M. H. Devoret. Dynamically protected cat-qubits: a new paradigm for universal quantum computation. *New Journal of Physics* **16**: 045014, 2014.

[61] R. G. Lyons. *Understanding Digital Signal Processing*. Pearson Education India, 2004.

[62] L. Spietz, K. W. Lehnert, I. Siddiqi, and R. J. Schoelkopf. Primary electronic thermometry using the shot noise of a tunnel junction. *Science* **300**: 1929–1932, 2003.

[63] L. Spietz, R. J. Schoelkopf, and P. Pari. Shot noise thermometry down to 10 mK. *Applied Physics Letters* **89**: 183123, 2006.

[64] M. Simoen. *Parametric interactions with signals and the vacuum*. PhD thesis. Chalmers University of Technology, 2015.

[65] R. H. Koch, J. Clarke, W. Goubau, J. M. Martinis, C. M. Pegrum, and D. J. Van Harlingen. Flicker (1/f) noise in tunnel junction dc SQUIDs. *Journal of Low Temperature Physics* **51**: 207–224, 1983.

[66] R. Adler. A study of locking phenomena in oscillators. *Proceedings of the IRE* **34**: 351–357, 1946.

[67] H. L. Stover and W. H. Steier. Locking of laser oscillators by light injection. *Applied Physics Letters* **8**: 91–93, 1966.

[68] S. Kaka, M. R. Pufall, W. H. Rippard, T. J. Silva, S. E. Russek, and J. A. Katine. Mutual phase-locking of microwave spin torque nano-oscillators. *Nature* **437**: 389–392, 2005.

[69] Y.-Y. Liu, J. Stehlik, M. J. Gullans, J. M. Taylor, and J. R. Petta. Injection locking of a semiconductor double-quantum-dot micromaser. *Physical Review A* **92**: 053802, 2015.

[70] M. C. Cassidy, A. Bruno, S. Rubbert, M. Irfan, J. Kammhuber, R. N. Schouten, A. R. Akhmerov, and L. P. Kouwenhoven. Demonstration of an ac Josephson junction laser. *Science* **355**: 939–942, 2017.

[71] Y. Nakamura, Y. A. Pashkin, and J. S. Tsai. Coherent control of macroscopic quantum states in a single-Cooper-pair box. *Nature* **398**: 786–788, 1999.

[72] D. Rosenberg, D. Kim, R. Das, D. Yost, S. Gustavsson, D. Hover, P. Krantz, A. Melville, L. Racz, G. O. Samach, S. J. Weber, F. Yan, J. L. Yoder, A. J. Kerman, and W. D. Oliver. 3D integrated superconducting qubits. *npj Quantum Information* **3**: 42, 2017.

[73] J. Kelly, R. Barends, A. Fowler, A. Megrant, E. Jeffrey, T. White, D. Sank, J. Mutus, B. Campbell, Y. Chen, Z. Chen, B. Chiaro, A. Dunsworth, I. C. Hoi, C. Neill, P. J. J. O'Malley, C. Quintana, P. Roushan, A. Vainsencher, A. N. Cleland, and J. M. Martinis. State preservation by repetitive error detection in a superconducting quantum circuit. *Nature* **519**: 66–69, 2015.

[74] J. Clarke and F. K. Wilhelm. Superconducting quantum bits. *Nature* **453**: 1031, 2008.

[75] J. Koch, M. Y. Terri, J. Gambetta, A. A. Houck, D. Schuster, J. Majer, A. Blais, M. H. Devoret, S. M. Girvin, and R. J. Schoelkopf. Charge-insensitive qubit design derived from the Cooper pair box. *Physical Review A* **76**: 042319, 2007.

[76] A. Wallraff, D. I. Schuster, A. Blais, L. Frunzio, R.-S. Huang, J. Majer, S. Kumar, S. M. Girvin, and R. J. Schoelkopf. Strong coupling of a single photon to a superconducting qubit using circuit quantum electrodynamics. *Nature* **431**: 162–167, 2004.

[77] P. Knight and G. Gerry. *Introductory Quantum Optics*. Cambridge University Press Cambridge, 2005.

[78] R. Schutjens, F. A. Dagga, D. J. Egger, and F. K. Wilhelm. Single-qubit gates in frequency-crowded transmon systems. *Physical Review A* **88**: 052330, 2013.

[79] R. Vijay, D. H. Slichter, and I. Siddiqi. Observation of quantum jumps in a superconducting artificial atom. *Physical Review Letters* **106**: 110502, 2011.

[80] Z. R. Lin, K. Inomata, W. D. Oliver, K. Koshino, Y. Nakamura, J. S. Tsai, and T. Yamamoto. Single-shot readout of a superconducting flux qubit with a flux-driven Josephson parametric amplifier. *Applied Physics Letters* **103**: 132602, 2013.

[81] F. Mallet, F. R. Ong, A. Palacios-Laloy, F. Nguyen, P. Bertet, D. Vion, and D. Esteve. Single-shot qubit readout in circuit quantum electrodynamics. *Nature Physics* **5**: 791–795, 2009.

[82] M. D. Reed, L. DiCarlo, B. R. Johnson, L. Sun, D. I. Schuster, L. Frunzio, and R. J. Schoelkopf. High-fidelity readout in circuit quantum electrodynamics using the Jaynes-Cummings nonlinearity. *Physical Review Letters* **105**: 173601, 2010.

[83] Z. R. Lin, K. Inomata, K. Koshino, W. D. Oliver, Y. Nakamura, J.-S. Tsai, and T. Yamamoto. Josephson parametric phase-locked oscillator and its application to dispersive readout of superconducting qubits. *Nature Communications* **5**, 2014.

[84] J. Gambetta, A. Blais, D. I. Schuster, A. Wallraff, L. Frunzio, J. Majer, M. H. Devoret, S. M. Girvin, and R. J. Schoelkopf. Qubit-photon interactions in a cavity: Measurement-induced dephasing and number splitting. *Physical Review A* **74**: 042318, 2006.

[85] J. Kelly, R. Barends, B. Campbell, Y. Chen, Z. Chen, B. Chiaro, A. Dunsworth, A. G. Fowler, I.-C. Hoi, E. Jeffrey, A. Megrant, J. Mutus, C. Neill, P. J. J. O'Malley, C. Quintana, P. Roushan, D. Sank, A. Vainsencher, J. Wenner, T. C. White, A. N. Cleland, and J. M. Martinis. Optimal quantum control using randomized benchmarking. *Physical Review Letters* **112**: 240504, 2014.